



Hierarchical p -version C^1 finite elements on quadrilateral and triangular domains with curved boundaries and their applications to Kirchhoff plates

Yang Wu | Yufeng Xing | Bo Liu

Institute of Solid Mechanics, Beihang University (BUAA), Beijing, China

Correspondence

Bo Liu, Institute of Solid Mechanics, Beihang University (BUAA), Beijing 100191, China.
Email: liubo68@buaa.edu.cn

Funding information

National Natural Science Foundation of China, Grant/Award Number: 11772031, 11402015, 11372021, and 11172028

Summary

This work focuses on the construction of p -version finite elements *that have curve boundaries* for C^1 problems. Both triangular and quadrilateral elements are constructed based on the C^1 -version blending function interpolation methods that are developed in this work and in the literature. Orthogonal hierarchical bases are constructed and subsequently transformed into interpolative nodal bases to facilitate the imposition of boundary conditions and the implementation of C^1 conformity on curvilinear domains. Nodal collocation strategies are also studied for improving the numerical performance, and novel nonuniformly distributed nodes, namely, Gauss-Jacobi (GJ) points, are proposed. For parallelograms and straight-sided triangular elements, C^1 continuity is exactly satisfied between neighboring elements. The difficulty of C^1 conformity for elements that have curved boundaries is circumvented by interpolating the normal derivatives at Gauss-Lobatto nodes. Moreover, with the help of the blending function interpolation method, the bases on edges and the internal modes can differ in terms of approximation order. Therefore, local p -refinements can be easily performed by these elements. Numerical results demonstrated that these elements are computationally inexpensive and converge fast for problems with regular and irregular domains.

KEYWORDS

C^1 conformity, curvilinear domains, hierarchical elements, Kirchhoff plates, local p -refinement

1 | INTRODUCTION

Finite elements that satisfy C^1 conformity requirements have been widely used in solving many scientific and engineering problems, such as problems that involve Euler-Bernoulli beams, Kirchhoff plates and shells, and incompressible flows.^{1–3} A tremendous amount of effort was devoted to the construction of h -version C^1 elements in early research. Typical examples of such elements are the nonconforming MZC rectangular elements, the conforming TUBA family of triangular elements, and the BFS rectangular elements.² They have been comprehensively reviewed in the work of Hrabok and Hrudey.⁴ These elements were originally constructed for the Kirchhoff plate problems. However, they have been found to be useful in many applications. For example, Dau et al⁵ developed a triangular sandwich shell element using the bases of Argyris' TUBA elements, and Holdeman⁶ proposed a Hermite finite-element method (FEM) for incompressible fluid flow, in which a series of C^1 bases, including the MZC bases, BFS bases, and blending function bases that were specified

by Watkins,⁷ were used as the stream functions. More recently, Lesičar et al⁸ proposed a second-order two-scale computational homogenization method for the modeling of large-strain deformations of heterogeneous material, where the bases of TUBA elements with 18 degrees of freedom (DOFs) were used for the discretization at the micro level.

Compared with the common h -version finite elements, p -version elements typically have a higher convergence rate and, hence, produce highly accurate results using fewer DOFs.⁹ However, the convergence rate of the p -version FEM may decline substantially if the domains of the problems are represented inaccurately. An illustrative example can be found in chapter 5 in the work of Stein et al.,¹⁰ where elements that have slightly inaccurate geometries cause the solutions to converge to erroneous results. Thus, for analyzing problems with irregular domains with high accuracy, p -version finite elements that have curved boundaries are essential.

Earlier literature regarding p -version C^1 elements can be found in the works of Peano,¹¹ Wang et al.,¹² and Chinosi et al.¹³ The bases were constructed via linear transformation of the monomials of Pascal's triangle or using rational functions. However, these studies were limited to straight-sided triangular elements. Bardell^{14,15} developed a series of hierarchical bases for rectangular elements using the tensor product of third-order Hermite bases, along with Legendre orthogonal polynomials, and applied the elements to vibration analyses of rectangular and skew plates. However, C^1 continuity of the elements was only satisfied for rectangular elements that had sides that were parallel to the global axis since the starting point of the bases was the BFS elements that have such a difficulty.¹⁶ Beslin and Nicolas¹⁷ developed a type of hierarchical bases using trigonometric functions and applied the bases to the prediction of very high-order plate bending modes. Their study was limited to analysis using a single patch due to the conformity difficulty, as in the work of Bardell. Xing and Liu¹⁸ developed a weak-form differential quadrature method (DQM) that uses tensor-product Lagrange bases that are based on nonuniformly distributed Gauss-Lobatto (GL) points for thin-plate vibration on curvilinear domains. The method was further improved by Zhong and Yue¹⁹ and Jin and Wang²⁰ via the combinational use of Lagrange and Hermite bases. Recently, Ferreira and Bittencourt²¹ proposed a new set of C^1 -conforming hierarchical bases for quadrangular and triangular elements. Their quadrilateral H_3 elements were also based on the BFS elements, like Bardell's elements, and the H_5 elements were derived from the tensor products of fifth-order Hermite bases that were enriched by high-order terms. The triangular bases were based on the TUBA elements and were enriched by tensor-product edge and face functions. Fast convergence of the elements was observed in thin-plate analyses. However, elements that had curved boundaries were not contained in their studies, and local refinement may propagate from element to element due to the use of tensor-product bases. In summary, most of the existing p -version C^1 elements are limited to the straight-side case. *The p-version C^1 elements that have curved boundaries, although important, are far from being fully developed.*

Compared with their C^0 counterparts, the construction of fully C^1 conforming elements that have curved boundaries was found to be difficult. The formulas may become very complicated, even when only one curved side is involved.^{22,23} The method of isogeometric analysis (IGA), which was introduced by Hughes et al.,²⁴ is a simple approach for tackling the problem of C^1 conformity within a single patch. Using the strategy of k -refinement,^{24,25} one can easily obtain the bases of high-order continuity. However, the advantage of adjusting the continuity order is limited to the interior of the patch. Due to the non-interpolative property of nonuniform rational basis spline (NURBS) bases and the rotation-free feature of control variables, the enforcement of C^1 conformity on patch boundaries is difficult, as in the FEM, and additional conformity-enhancement techniques are often employed. For example, Kiendl et al^{26,27} and Shojaee et al²⁸ employed the NURBS bases to analyze the Kirchhoff shells and plates. The C^1 conformity between patches was approximately satisfied by using the bending strip method, where a penalty factor for rotation discontinuity was introduced. The penalty factor should be selected carefully such that the global stiffness matrix does not become poorly conditioned.²⁷ Guo and Ruess²⁹ and Guo et al³⁰ used Nitsche's method to enforce the C^1 conformity in an integral sense and applied it to the NURBS-based IGA of Krichhoff shells. However, compared with the conventional FEM, this method is complex. To overcome the limitations of NURBS-based IGA, Liu et al³¹ constructed nonuniform rational Hermite functions for C^0 and C^1 IGA. However, they encountered the same difficulties as with the C^1 tensor-product Hermite elements.^{14,15} Sustained efforts are required in the development of simpler methods for enforcing the C^1 conformity.

In this context, p -version C^1 elements with curved edges were constructed via the method of Hermite blending function interpolation. First, conventional hierarchical bases were proposed for both quadrilateral and triangular elements. These bases were constructed through the Jacobi orthogonal polynomials and the blending function interpolation. Due to the lack of a collocation property, these bases cannot be applied directly to the imposition of boundary conditions or to element assembly for elements that have curved boundaries. Therefore, a linear transformation was employed to transform these non-interpolative bases into nodal bases, where nodal collocation strategies were studied to improve the matrix conditioning. For parallelograms and straight-sided triangular elements, C^1 conformity is exactly satisfied along the element boundary. For elements that have curved boundaries, including distorted straight-sided quadrilateral elements, the

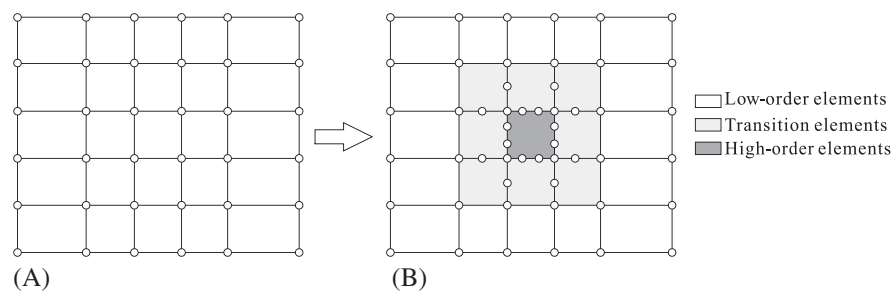


FIGURE 1 Local p -refinement. A, Initial mesh; B, Local p -refinement

continuity of deflection is exactly satisfied, whereas the continuity of normal derivatives is approximately satisfied by a highly accurate interpolation at GL nodes. *In this way, the element assembly (the enforcement of C^1 conformity) can be implemented in the typical manner without using additional enhancement techniques, such as those in IGA, and fast convergence can still be realized (as will be demonstrated).* Moreover, because of the advantages of blending function interpolation, the approximation orders for w (a field variable) and w_n (the normal derivative of w) on each edge are independent, which enables these elements to perform a local p -refinement (Figure 1) that is not available for many tensor-product elements.^{14,15,17,18,24} In addition, the independence property enables one to improve the continuity level of normal derivatives by adding nodes only for w_n . This was demonstrated to be very powerful in the improvement of C^1 conformity on curved boundaries, along with the corresponding convergence rate.

The remainder of this paper is organized as follows. First, the Hermite blending function interpolation methods on square and triangular domains are introduced in Section 2. Then, the hierarchical bases for these quadrilateral and triangular elements are constructed in Sections 3 and 4, respectively. The implementation details of these elements are presented in Section 5, and numerical examples are presented in Section 6. Finally, the conclusions of this work are discussed in Section 7.

2 | HERMITE BLENDING FUNCTION INTERPOLATION

The FEM shape functions can be constructed intuitively if one is familiar with the interpolative properties of the shape functions. It is easy to construct these functions when the topology of the elements and the conformity requirements are simple. However, the construction of C^1 elements is not easy since high-order derivatives are often involved in the nodal variables. Therefore, the Hermite blending function interpolation method, which is introduced in this section, will be used to construct the shape functions (the vertex and edge bases only; see the next section). The formulas for a unit square domain can be found in the work of Gordon,³² which were used by Watkins⁷ to construct the conforming rectangular elements. They are included here for completeness. Inspired by the works of Gordon³² and Gordon and Hall,³³ formulas for a triangular domain are derived by the authors of this work.

2.1 | Blending function interpolation on a unit square domain

As shown in Figure 2A, consider a smooth function $F(\xi, \eta)$ that is defined on a unit square domain with the following boundary functions of values and derivatives:

$$\begin{aligned} f_1(\xi) &= F(\xi, -1), f_2(\eta) = F(1, \eta), f_3(\xi) = F(\xi, 1), f_4(\eta) = F(-1, \eta) \\ g_1(\xi) &= F_\eta(\xi, -1), g_2(\eta) = F_\xi(1, \eta), g_3(\xi) = F_\eta(\xi, 1), g_4(\eta) = F_\xi(-1, \eta), \end{aligned} \quad (1)$$

where F_ξ and F_η denote the first-order partial derivatives with respect to ξ and η . The Hermite blending function interpolation can be used to find an approximation function, which is denoted as $\tilde{F}(\xi, \eta)$, that has the same boundary functions of values and derivatives as $F(\xi, \eta)$. To this end, the following third-order Hermite interpolation bases are often used:

$$\begin{aligned} h_1(\xi) &= \frac{1}{4}(\xi + 1)(\xi - 1)^2, & h_2(\xi) &= \frac{1}{4}(\xi + 2)(\xi - 1)^2 \\ h_3(\xi) &= \frac{1}{4}(2 - \xi)(\xi + 1)^2, & h_4(\xi) &= \frac{1}{4}(\xi - 1)(\xi + 1)^2, \end{aligned} \quad (2)$$

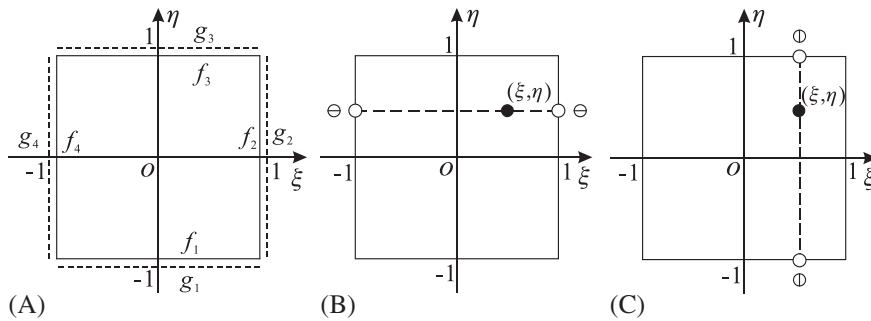


FIGURE 2 Blending function interpolation on a unit square domain. A, Boundary functions of values and derivatives; B, Interpolation along the ξ -direction; C, Interpolation along the η -direction

where h_1 and h_4 are attached to the derivatives at the two ends of $[-1, 1]$ and h_2 and h_3 are attached to the function values at the ends. By interpolating F along the ξ -direction (see Figure 2B), one can obtain

$$P_\xi[F] = g_4(\eta) h_1(\xi) + f_4(\eta) h_2(\xi) + f_2(\eta) h_3(\xi) + g_2(\eta) h_4(\xi), \quad (3)$$

where $P_\xi[\cdot]$ is the projection operator³² that is related to the ξ -direction. $P_\xi[F]$ has the same boundary values and derivatives as F on edges $\xi = \pm 1$. Therefore, the interpolation residual, which is denoted as R and defined as

$$R = F - P_\xi[F], \quad (4)$$

has zero values and normal derivatives on $\xi = \pm 1$. By interpolating R in the η -direction (see Figure 2C), one can obtain

$$P_\eta[R] = R(\xi, -1) h_1(\eta) + R_\eta(\xi, -1) h_2(\eta) + R(\xi, 1) h_3(\eta) + R_\eta(\xi, 1) h_4(\eta), \quad (5)$$

where $P_\eta[\cdot]$ is the projection operator that is related to the η -direction and R_η is the partial derivative of R with respect to η . $P_\eta[R]$ also has zero values and normal derivatives on $\xi = \pm 1$, whereas the values and normal derivatives on $\eta = \pm 1$ are the same as those of R . Finally, one can conclude that

$$\tilde{F} = P_\xi[F] + P_\eta[R] \quad (6)$$

is the desired approximation that has the same boundary values and derivatives as F . According to Equation (3), the projection operators are linear. It follows that

$$P_\eta[R] = P_\eta[F - P_\xi[F]] = P_\eta[F] - P_\eta[P_\xi[F]]. \quad (7)$$

The projection operators are also commutative,³² which implies $P_\eta[P_\xi[F]] = P_\xi[P_\eta[F]]$ or, for simplicity, $P_\eta P_\xi[F] = P_\xi P_\eta[F]$. Substituting Equation (7) into Equation (6), the approximation function can be expressed as

$$\tilde{F} = P_\xi[F] + P_\eta[F] - P_\xi P_\eta[F], \quad (8)$$

where

$$\begin{aligned} P_\xi[F] &= g_4(\eta) h_1(\xi) + f_4(\eta) h_2(\xi) + f_2(\eta) h_3(\xi) + g_2(\eta) h_4(\xi) \\ P_\eta[F] &= g_1(\xi) h_1(\eta) + f_1(\xi) h_2(\eta) + f_3(\xi) h_3(\eta) + g_3(\xi) h_4(\eta) \\ P_\xi P_\eta[F] &= [g'_1(-1) h_1(\eta) + f'_1(-1) h_2(\eta) + f'_3(-1) h_3(\eta) + g'_3(-1) h_4(\eta)] h_1(\xi) \\ &\quad + [g_1(-1) h_1(\eta) + f_1(-1) h_2(\eta) + f_3(-1) h_3(\eta) + g_3(-1) h_4(\eta)] h_2(\xi) \\ &\quad + [g_1(1) h_1(\eta) + f_1(1) h_2(\eta) + f_3(1) h_3(\eta) + g_3(1) h_4(\eta)] h_3(\xi) \\ &\quad + [g'_1(1) h_1(\eta) + f'_1(1) h_2(\eta) + f'_3(1) h_3(\eta) + g'_3(1) h_4(\eta)] h_4(\xi). \end{aligned} \quad (9)$$

For more details about the blending function interpolation, one may refer to the work of Gordon.³² An example of verifying the interpolation properties of the method is shown in Figure 3. The errors at all boundaries vanish; hence, all the boundary conditions in Equation (1) are well satisfied.

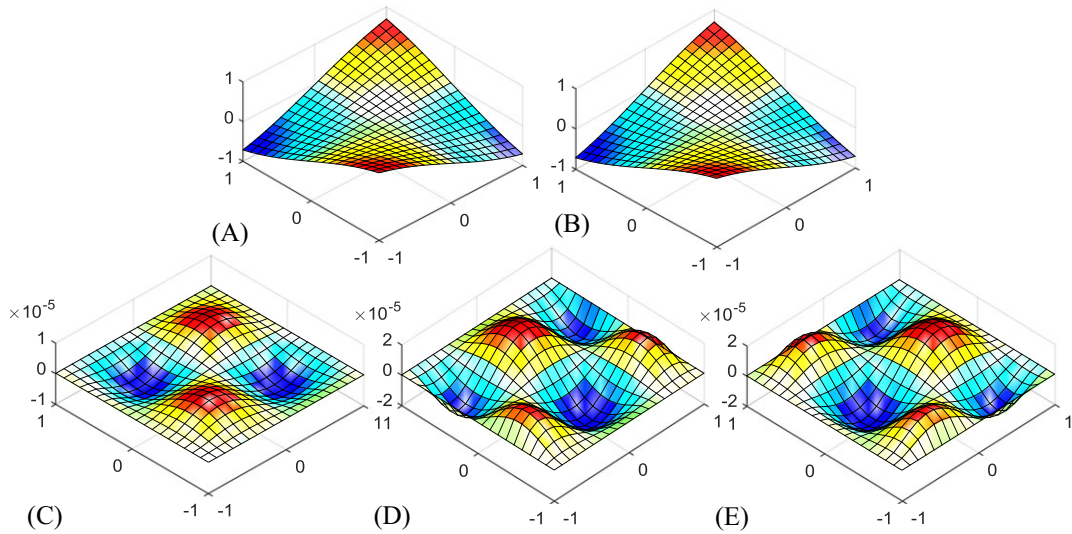


FIGURE 3 Interpolation on a unit square domain. A, $F = \sin(\xi) \sin(\eta)$; B, \tilde{F} ; C, $F - \tilde{F}$; D, $\partial F / \partial \xi - \partial \tilde{F} / \partial \xi$; E, $\partial F / \partial \eta - \partial \tilde{F} / \partial \eta$

2.2 | Blending function interpolation on a unit triangular domain

Consider a two-dimensional function, namely, $F(\xi, \eta)$, that is defined on a unit triangular domain (see Figure 4A) and has the following boundary functions of values and derivatives:

$$\begin{aligned} f_1(\xi) &= F(\xi, 0), f_2(\eta) = F(1 - \eta, \eta), f_3(\eta) = F(0, \eta) \\ g_1(\xi) &= F_\eta(\xi, 0), g_2(\eta) = F_\xi(1 - \eta, \eta), g_3(\eta) = F_\xi(0, \eta). \end{aligned} \quad (10)$$

Function g_2 is no longer the normal derivative of F on the bevel edge. In contrast to the square domain, the Hermite interpolation functions on the triangular domain should be rational because of the bevel edge. For example, the interpolation functions, namely, ϕ_i , for the ξ -direction (see Figure 4B) are expressed as

$$\begin{aligned} \phi_1(\xi, \eta) &= \frac{\xi(\xi + \eta - 1)^2}{(1 - \eta)^2}, \quad \phi_2(\xi, \eta) = \frac{(\xi + \eta - 1)^2(2\xi + 1 - \eta)}{(1 - \eta)^3} \\ \phi_3(\xi, \eta) &= \frac{\xi^2(2\xi - 3 + 3\eta)}{(\eta - 1)^3}, \quad \phi_4(\xi, \eta) = \frac{(\xi + \eta - 1)\xi^2}{(1 - \eta)^2}, \end{aligned} \quad (11)$$

where ϕ_1 and ϕ_4 are attached to the derivatives at the two ends of a line segment in the ξ -direction and ϕ_2 and ϕ_3 are attached to the function values at the two ends. Similarly, the interpolation functions, namely, ψ_i , for the η -direction (see Figure 4C) can be easily obtained by exchanging the variables of ϕ_i in Equation (11), as follows:

$$\begin{aligned} \psi_1(\xi, \eta) &= \phi_1(\eta, \xi), \quad \psi_2(\xi, \eta) = \phi_2(\eta, \xi) \\ \psi_3(\xi, \eta) &= \phi_3(\eta, \xi), \quad \psi_4(\xi, \eta) = \phi_4(\eta, \xi), \end{aligned} \quad (12)$$

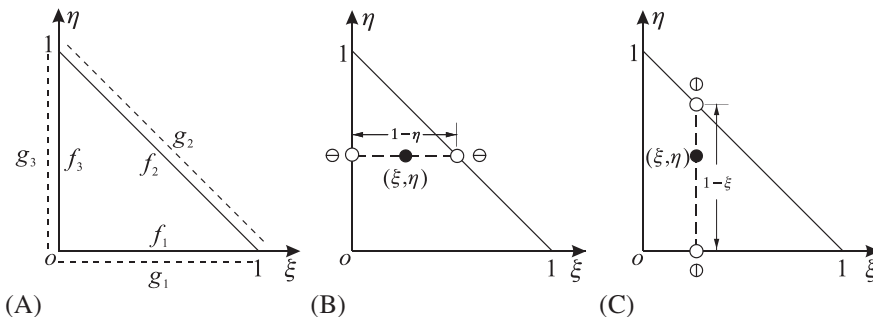


FIGURE 4 Blending function interpolation on a unit triangular domain. A, Boundary functions of values and derivatives; B, Interpolation along the ξ -direction; C, Interpolation along the η -direction

where ψ_1 and ψ_4 are attached to the derivatives (with respect to η) at the two ends of a line segment in the η -direction and ψ_2 and ψ_3 are related to the function values at the two ends. Following the same procedure as in Section 2.1 and interpolating F in the ξ -direction yields

$$P_\xi[F] = g_3(\eta)\phi_1 + f_3(\eta)\phi_2 + f_2(\eta)\phi_3 + g_2(\eta)\phi_4. \quad (13)$$

Then, the residual, namely, R , is expressed as

$$R = F - P_\xi[F] \quad (14)$$

and

$$P_\eta[R] = R_\eta(\xi, 0)\psi_1 + R(\xi, 0)\psi_2 + R(\xi, 1 - \xi)\psi_3 + R_\eta(\xi, 1 - \xi)\psi_4. \quad (15)$$

Since $P_\xi[F]$ and F share the same function value and partial derivative with respect to ξ on the bevel edge, it follows that $P_\xi[F]$ and F also have the same function value and partial derivative with respect to η on that edge, which implies $R(\xi, 1 - \xi) = R_\eta(\xi, 1 - \xi) = 0$ in Equation (15). Define another projection operator of R in the η -direction, as follows:

$$\tilde{P}_\eta[R] = R_\eta(\xi, 0)\psi_1 + R(\xi, 0)\psi_2. \quad (16)$$

Then,

$$P_\eta[R] = \tilde{P}_\eta[R] = \tilde{P}_\eta[F] - \tilde{P}_\eta P_\xi[F], \quad (17)$$

and the final approximation function, namely, \tilde{F} , can be expressed as

$$\tilde{F} = P_\xi[F] + P_\eta[R] = P_\xi[F] + \tilde{P}_\eta[F] - \tilde{P}_\eta P_\xi[F], \quad (18)$$

where

$$\begin{aligned} P_\xi[F] &= g_3(\eta)\phi_1 + f_3(\eta)\phi_2 + f_2(\eta)\phi_3 + g_2(\eta)\phi_4 \\ P_\eta[F] &= g_1(\xi)\psi_1 + f_1(\xi)\psi_2 \\ \tilde{P}_\eta P_\xi[F] &= \psi_1 \left[\begin{array}{l} g'_3(0)\phi_1(\xi, 0) + f'_3(0)\phi_2(\xi, 0) + f'_2(0)\phi_3(\xi, 0) + g'_2(0)\phi_4(\xi, 0) + \\ g_3(0)\phi'_{1,\eta}(\xi, 0) + f_3(0)\phi'_{2,\eta}(\xi, 0) + f_2(0)\phi'_{3,\eta}(\xi, 0) + g_2(0)\phi'_{4,\eta}(\xi, 0) \end{array} \right] \\ &\quad + \psi_2 [g_3(0)\phi_1(\xi, 0) + f_3(0)\phi_2(\xi, 0) + f_2(0)\phi_3(\xi, 0) + g_2(0)\phi_4(\xi, 0)]. \end{aligned} \quad (19)$$

As verified in Figure 5, the approximation function \tilde{F} has the same function values and two partial derivatives on the boundaries as the specified function F .

Using the interpolation method in Equations (8) and (18), one can construct a two-dimensional function with prescribed boundary functions, which is the main strategy for the construction of shape functions in this work. The blending function interpolation is valid only if F is sufficiently smooth; hence, the boundary functions should be sufficiently consistent.

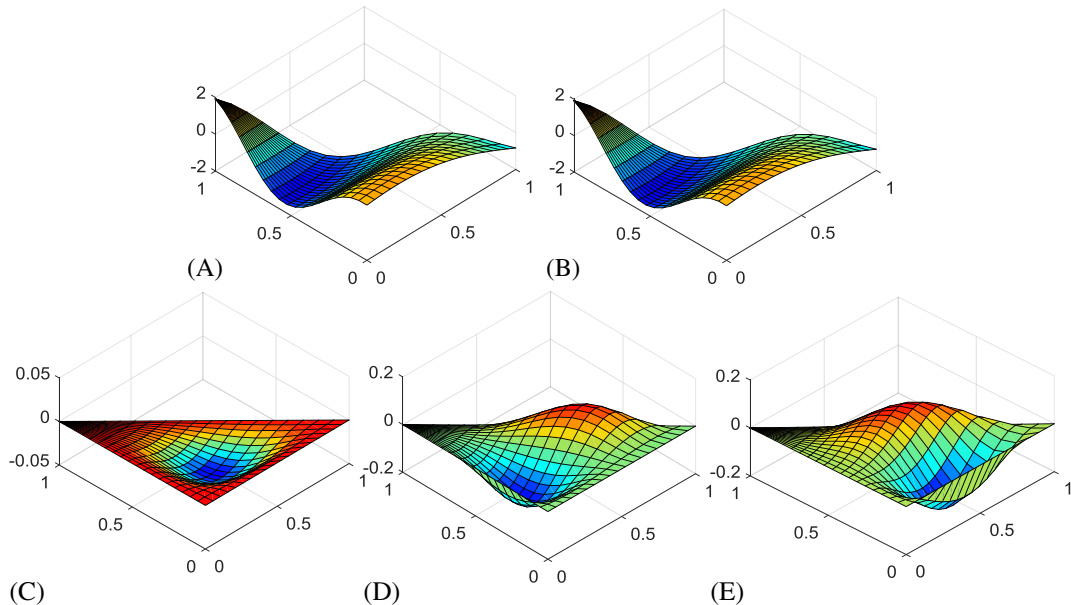


FIGURE 5 Interpolation on a unit triangular domain. A, $F = (1 + \xi + \eta) \cos(2\xi) \cos(6\eta)$; B, \tilde{F} ; C, $F - \tilde{F}$; D, $\partial F / \partial \xi - \partial \tilde{F} / \partial \xi$; E, $\partial F / \partial \eta - \partial \tilde{F} / \partial \eta$

For example, on the corner ($\xi = 0, \eta = 0$), the specified functions should satisfy $f_1(0) = f_3(0)$, $f'_3(0) = g_1(0)$, etc. Evaluating the consistency is tedious. However, this difficulty will not be encountered during element construction in this work since the boundary functions are interpolated by the nodal variables, and the consistency is satisfied automatically.

3 | HIERARCHICAL BASES FOR QUADRILATERAL ELEMENTS

In this section, hierarchical bases for quadrilateral elements will be developed. The boundary shape functions, including vertex and edge functions, are derived using the blending function interpolation in Section 2.1, whereas the face functions are constructed via tensor production of one-dimensional bases in the ξ - and η -directions. Function F in Section 2 is replaced by displacement variable w in the following discussions (including Section 4).

3.1 | Vertex functions

To derive the shape functions using the blending function interpolation method, the boundary functions in Equation (1) should be determined first. As shown in Figure 6, six nodal variables are used on each vertex. The boundary normal derivatives, which are denoted as w_n (namely, g_i in Equation (1)), can be interpolated by the third-order Hermite bases in Equation (2), along with two variables on each end. For example, the variables for the interpolation of g_1 on vertices 1 and 2 are $\partial w/\partial\eta$ and $\partial^2 w/\partial\xi\partial\eta$. Similarly, the boundary value of w (namely, f_i in Equation (1)) on each side can be interpolated by the fifth-order Hermite bases that are expressed in Equation (20) and three variables are used at each end. For example, the related variables for the interpolation of f_1 are w , $\partial w/\partial\xi$ and $\partial^2 w/\partial\xi^2$ on vertices 1 and 2.

$$\begin{aligned} H_1^{(2)} &= (1 - \xi)^3(1 + \xi)^2/16 & H_2^{(2)} &= (1 + \xi)^3(1 - \xi)^2/16 \\ H_1^{(1)} &= (1 - \xi)^3(1 + \xi)(5 + 3\xi)/16 & H_2^{(1)} &= (1 + \xi)^3(\xi - 1)(5 - 3\xi)/16 \\ H_1 &= (1 - \xi)^3(3\xi^2 + 9\xi + 8)/16 & H_2 &= (1 + \xi)^3(3\xi^2 - 9\xi + 8)/16 \end{aligned} \quad (20)$$

After the boundary functions in Equation (1) have been determined, the shape functions can be obtained directly via Equations (8) and (9). To determine the shape function for each nodal variable, one can set the variable to 1 and all other nodal variables to zero, and the corresponding shape function can be obtained via the blending function interpolation procedure. For example, to determine the shape function that is attached to variable w on vertex 1 (denoted by w^{V1}), we set $w^{V1} = 1$ and all other nodal variables on the vertex and other vertices to zero. Then, the boundary functions in Equation (1) can be interpolated as

$$f_1 = H_1(\xi); f_4 = H_1(\eta); f_2 = f_3 = g_1 = \dots = g_4 = 0. \quad (21)$$

Using the blending function interpolation in Equation (8), the corresponding shape function can be obtained as

$$S_w^{V1} = H_1(\eta)h_2(\xi) + H_1(\xi)h_2(\eta) - h_2(\xi)h_2(\eta). \quad (22)$$

Using similar procedures, one can obtain the other shape functions on the remaining vertices. The shape functions at vertex 1 are plotted in Figure 7.

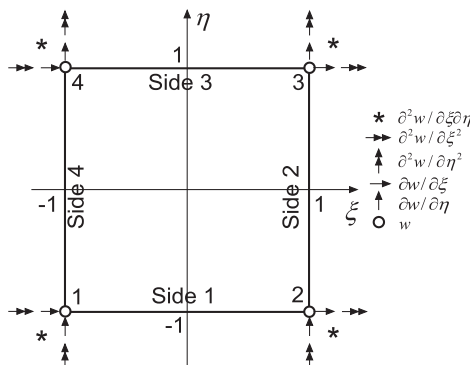


FIGURE 6 Vertex degree-of-freedom collocation for a unit quadrilateral element

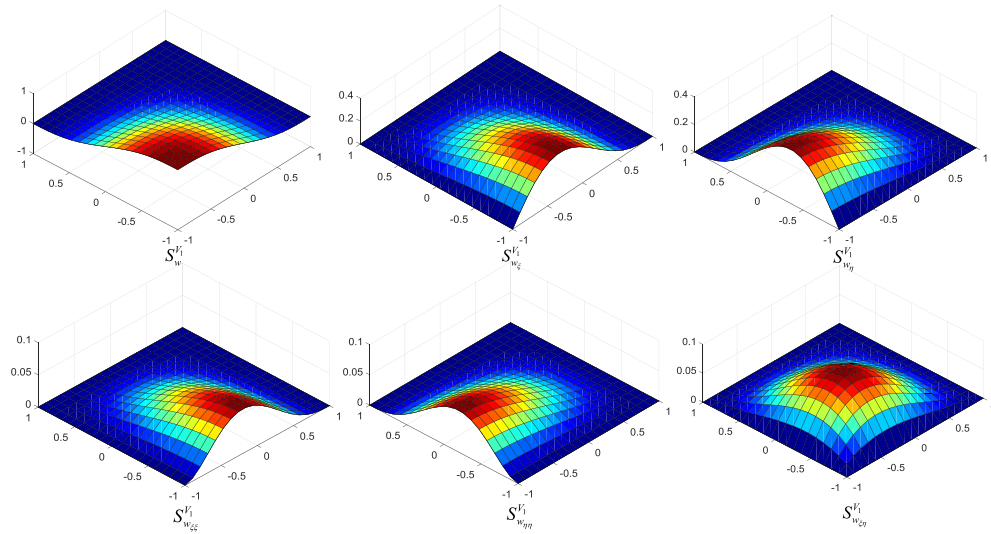


FIGURE 7 Vertex functions for a unit quadrilateral element at vertex 1

3.2 | Edge functions

The edge functions for C^1 elements can be divided into two parts: (i) bases for the enrichment of boundary values, namely, w , that have zero normal derivatives and (ii) bases for the enrichment of boundary normal derivatives, namely, w_n , that have zero function values. According to Section 3.1, the boundary functions for w and w_n are complete up to the fifth and third orders, respectively. Therefore, the enriching bases for w and w_n should start from the sixth and fourth orders. Taking side 1 as an example, we let

$$f_i = (1 + \xi)^3(1 - \xi)^3 J_i^{(\alpha, \beta)}(\xi), \quad i = 0, 1, \dots, \quad (23)$$

where $J_i^{(\alpha, \beta)}$, $i = 0, 1, \dots$, are the Jacobi polynomials and the weights (α, β) are set as $(4, 4)$ in accordance with the internal modes (see the next section) so that the bases can be calculated together. By forcing the other boundary functions in Equation (1) to be zero and using Equation (8), one can obtain the edge functions for w on side 1 as

$$S_{w,i}^{S_1} = (1 + \xi)^3(1 - \xi)^3 J_i^{(4,4)}(\xi) h_2(\eta), \quad i = 0, 1, \dots. \quad (24)$$

To improve the computational efficiency, using the recursion formulas of Jacobi polynomials to calculate the bases and their derivatives is highly recommended. Thus, we have

$$a_n J_n^{(\alpha, \beta)}(x) = (b_n x + c_n) J_{n-1}^{(\alpha, \beta)}(x) - d_n J_{n-2}^{(\alpha, \beta)}(x) \quad (25)$$

$$\frac{d}{dx} J_n^{(\alpha, \beta)}(x) = \frac{n + \alpha + \beta + 1}{2} J_{n-1}^{(\alpha+1, \beta+1)}(x), \quad J_{-1}^{(\alpha, \beta)}(x) = 0, \quad (26)$$

where

$$\begin{aligned} a_n &= 2n(\alpha + \beta + n)(\alpha + \beta + 2n - 2) \\ b_n &= (\alpha + \beta + 2n - 2)(\alpha + \beta + 2n - 1)(\alpha + \beta + 2n) \\ c_n &= (\alpha + \beta + 2n - 1)(\alpha^2 - \beta^2) \\ d_n &= 2(\alpha + n - 1)(\beta + n - 1)(\alpha + \beta + 2n). \end{aligned} \quad (27)$$

These formulas can be found in mathematics handbooks. They are included here for completeness. Similarly, the edge functions that correspond to the normal derivatives are expressed as

$$S_{w_n,i}^{S_1} = (1 + \xi)^2(1 - \xi)^2 J_i^{(4,4)}(\xi) h_1(\eta), \quad i = 0, 1, 2, \dots. \quad (28)$$

The edge functions on other sides can be derived via similar approaches. The numbers of edge functions on the four sides can differ; therefore, joining elements that have different polynomial degrees is possible. Moreover, the numbers of edge functions for w and w_n on the same side can also differ; hence, the approximation orders for w and w_n on the boundaries are independent. As will be shown in Section 6.3, this property is beneficial for enhancing the C^1 conformity on curved edges. Figure 8 shows the first three edge functions for w and w_n .

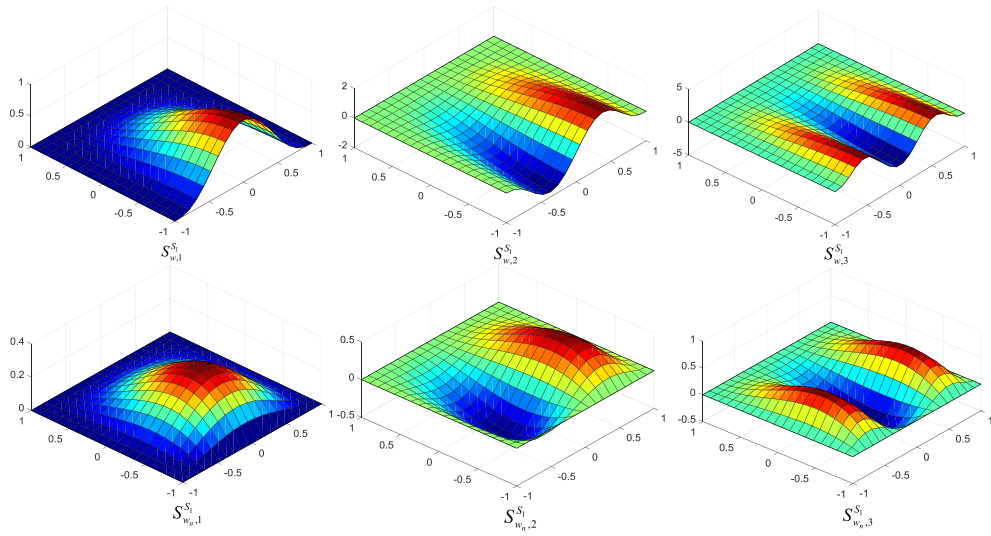


FIGURE 8 Edge functions for a unit quadrilateral element

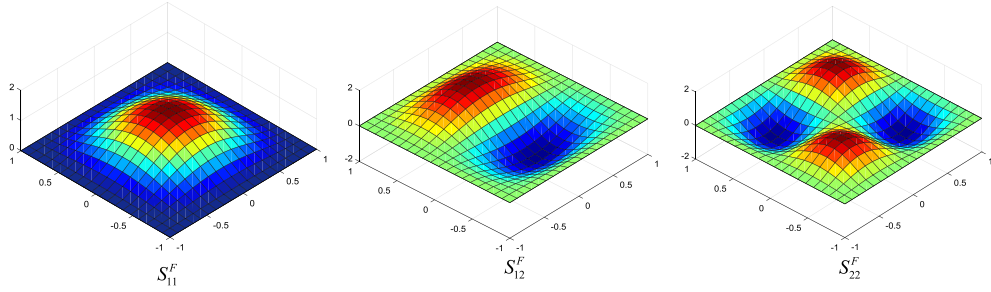


FIGURE 9 First three face functions for a unit quadrilateral element

3.3 | Face functions

The face functions of quadrilateral elements can be obtained by simply calculating the tensor product of one-dimensional C^1 hierarchical bases as follows:

$$S_{mn}^F = C_{mn} (1 - \xi^2)^2 (1 - \eta^2)^2 J_{m-1}^{(4,4)}(\xi) J_{n-1}^{(4,4)}(\eta), \quad m = 1, 2, \dots, H_\xi, n = 1, 2, \dots, H_\eta$$

$$C_{mn} = \frac{1}{2^9} \sqrt{(2m+7)(2n+7) \prod_{i=4}^7 (m+i) \prod_{j=4}^7 (n+j) / \prod_{i=0}^3 (m+i) \prod_{j=0}^3 (n+j)}, \quad (29)$$

where m and n are the indices and H_ξ and H_η are the numbers of bases along each direction of the natural coordinates. The coefficients, which are denoted as C_{mn} , of the Jacobi polynomials are determined by the orthogonality requirement, ie,

$$\int_{-1}^1 \int_{-1}^1 S_{pq}^F S_{mn}^F d\xi d\eta = \delta_{pm} \delta_{qn}, \quad (30)$$

where δ_{pm} and δ_{qn} are Kronecker deltas. The first three face functions are shown in Figure 9. According to Equation (29), both the function values and the normal derivatives of the bases vanish on the element boundaries. Appendix summarizes all the shape functions for the quadrilateral elements.

4 | HIERARCHICAL BASES FOR TRIANGULAR ELEMENTS

4.1 | Vertex functions

A similar process to that in Section 3.1 can be used to obtain the shape functions on a unit triangular domain. However, the vertex functions on vertices 2 and 3 should be determined carefully since the angles are no longer right

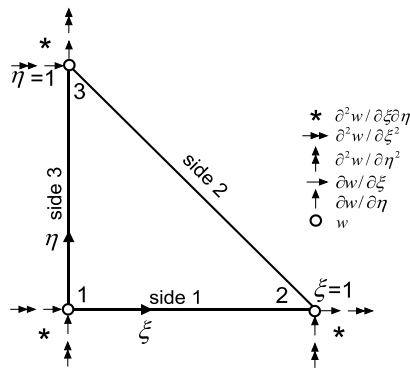


FIGURE 10 Vertex degree-of-freedom collocation of a unit triangular element

angles as in quadrilateral elements (see Figure 10). To obtain the boundary functions, the fifth-order Hermite polynomials in Equation (20), which are defined in $[-1, 1]$, are shifted to $[0, 1]$, ie,

$$\begin{aligned}\tilde{H}_1^{(2)}(\eta) &= (1 - \eta)^3 \eta^2 / 2 & \tilde{H}_2^{(2)}(\eta) &= \eta^3 (1 - \eta)^2 / 2 \\ \tilde{H}_1^{(1)}(\eta) &= (1 - \eta)^3 \eta (3\eta + 1) & \tilde{H}_2^{(1)}(\eta) &= \eta^3 (\eta - 1) (4 - 3\eta) \\ \tilde{H}_1(\eta) &= (1 - \eta)^3 (6\eta^2 + 3\eta + 1) & \tilde{H}_2(\eta) &= \eta^3 (6\eta^2 - 15\eta + 10).\end{aligned}\quad (31)$$

We derive the shape functions for w_η (which abbreviates $\partial w / \partial \eta$) at vertex 3 (denoted by $w_{\eta}^{V_3}$) as an example. First, let $w_{\eta}^{V_3} = 1$ and the remaining nodal variables be zero. Then, the boundary functions on sides 1 and 3 can be interpolated directly as

$$f_3(\eta) = \tilde{H}_2^{(1)}(\eta), \quad g_3(\eta) = f_1(\eta) = g_1(\eta) = 0. \quad (32)$$

To determine the boundary functions on side 2, the following relations (which follow from Equation (10)) should be used:

$$\begin{aligned}f_2(1) &= w_{\eta}^{V_3}, & f'_2(1) &= w_{\eta}^{V_3} - w_{\xi}^{V_3}, & f''_2(1) &= w_{\xi\xi}^{V_3} - 2w_{\xi\eta}^{V_3} + w_{\eta\eta}^{V_3} \\ g_2(1) &= w_{\xi}^{V_3}, & g'_2(1) &= w_{\xi\eta}^{V_3} - w_{\xi\xi}^{V_3}.\end{aligned}\quad (33)$$

As $w_{\eta}^{V_3}$ is assumed to be 1 and all other variables are assumed to be zero, Equation (33) becomes

$$f_2(1) = 0, \quad f'_2(1) = 1, \quad f''_2(1) = 0, \quad g_2(1) = 0, \quad g'_2(1) = 0. \quad (34)$$

On vertex 2, we have $f_2(0) = f'_2(0) = f''_2(0) = g_2(0) = g'_2(0) = 0$. Finally, boundary functions f_2 and g_2 can be interpolated by fifth- and third-order Hermite bases as

$$f_2(\eta) = \tilde{H}_2^{(1)}(\eta), \quad g_2(\eta) = 0. \quad (35)$$

Substituting Equations (32) and (35) into Equation (18), one can obtain the shape function for $w_{\eta}^{V_3}$ as

$$S_{w_{\eta}}^{V_3} = H_2^{(1)}(\eta) [\phi_2(\xi, \eta) + \phi_3(\xi, \eta)], \quad (36)$$

which can be simplified to

$$S_{w_{\eta}}^{V_3} = -\eta^3 (3\eta^2 - 7\eta + 4). \quad (37)$$

Similarly, one can derive the vertex functions for other nodal variables. The shape functions at vertex 3 are plotted in Figure 11. Equation (33) is essential for constructing shape functions that have consistent boundary functions, and it is even more important for the construction of shape functions for nodal variables such as $w_{\xi\xi}$, $w_{\xi\eta}$, and $w_{\eta\eta}$ at vertices 2 and 3 since these variables are coupled with both boundary values and the derivatives (see Equation (10)).

4.2 | Edge functions

The derivation of edge functions is also similar. For example, to derive the edge functions for w on side 1, one can consider

$$f_1 = \xi^3 (1 - \xi)^3 P_i(\xi), \quad i = 0, 1, \dots, \quad (38)$$

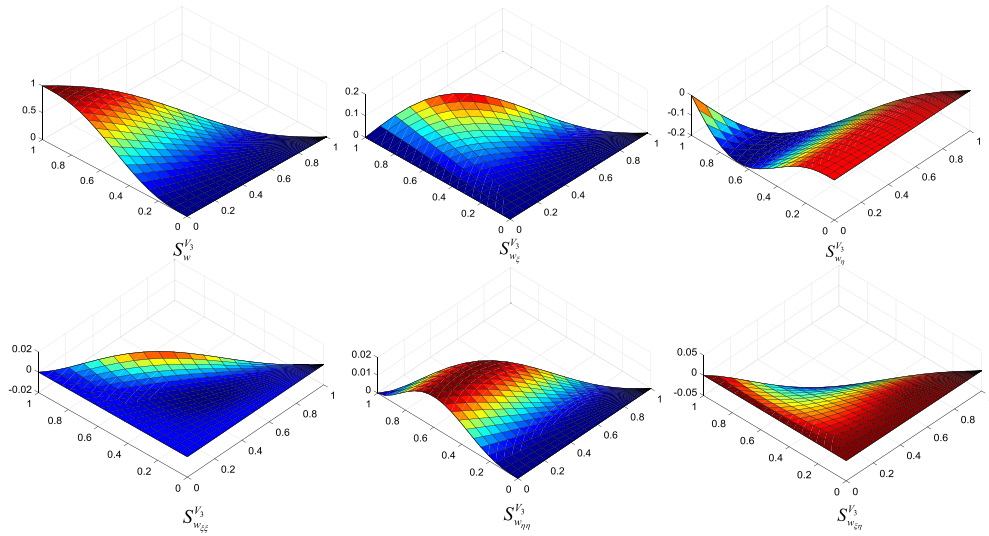


FIGURE 11 Vertex functions for a unit triangular element on vertex 3

where $P_i(\xi)$ is an unknown polynomial of order i . The other boundary functions in Equation (10) are set to zero. Then, the corresponding edge functions can be expressed as

$$S_{w,i}^{S_1}(\xi) = \xi^3(1-\xi)^3 P_i(\xi) \psi_2(\xi, \eta), \quad i = 0, 1, \dots. \quad (39)$$

Theoretically, P_i can be any group of complete polynomials. To improve the numerical properties of the basis transformation (see Section 5.1), P_i is determined by the orthogonality condition

$$\int_A S_{w,i}^{S_1} S_{w,j}^{S_1} dA = C \delta_{ij}, \quad (40)$$

where C is a constant and δ_{ij} is the Kronecker delta. It follows that

$$P_i(\xi) = J_i^{(7,6)}(2\xi - 1). \quad (41)$$

Therefore, the edge functions for w on side 1 can be expressed as

$$S_{w,i}^{S_1}(\xi) = \xi^3(\xi + \eta - 1)^2(2\eta + 1 - \xi) J_i^{(7,6)}(2\xi - 1), \quad i = 0, 1, 2, \dots. \quad (42)$$

Similarly, the edge functions for w_η at side 1 are

$$S_{w_\eta,i}^{S_1}(\xi) = \xi^2 \eta (\xi + \eta - 1)^2 J_i^{(7,4)}(2\xi - 1), \quad i = 0, 1, 2, \dots. \quad (43)$$

The edge functions on other sides can be derived in similar ways. The first three edge functions for w and w_η on side 1 are plotted in Figure 12.

4.3 | Face functions

The orthogonal face functions of these triangular elements are developed from the techniques for deriving the C^0 bases in the work of Webb and Abouchacra.³⁴ Neglecting the derivation steps, they are expressed as

$$S_{pn}^F(\xi, \eta) = C_{pn}(1 - \xi - \eta)^2 \xi^2 \eta^2 (1 - \eta)^{p-n-6} J_{p-n-6}^{(4,4)} \left(\frac{2\xi}{1 - \eta} - 1 \right) J_n^{(2p-2n-3,4)}(2\eta - 1), \quad (44)$$

where p (≥ 6) is the polynomial order and $n = 0, 1, \dots, p - 6$ are the indices of the p th-order face functions. The constant, namely, C_{pn} , is determined from the normalization condition in Equation (30) as

$$C_{pn} = \sqrt{(2p - 2n - 3)(2p + 2) \prod_{i=1}^4 (p - n - 2 + i)(2p - n - 3 + i) / \prod_{i=1}^4 (p - n - 6 + i)(n + i)}. \quad (45)$$

The number of linearly independent p th-order face functions is $p - 5$. For a specified order $p \geq 6$, the number of complete face functions is $N_f = (p - 4)(p - 5)/2$. The rational term in Equation (44) is eliminated automatically. The first three face

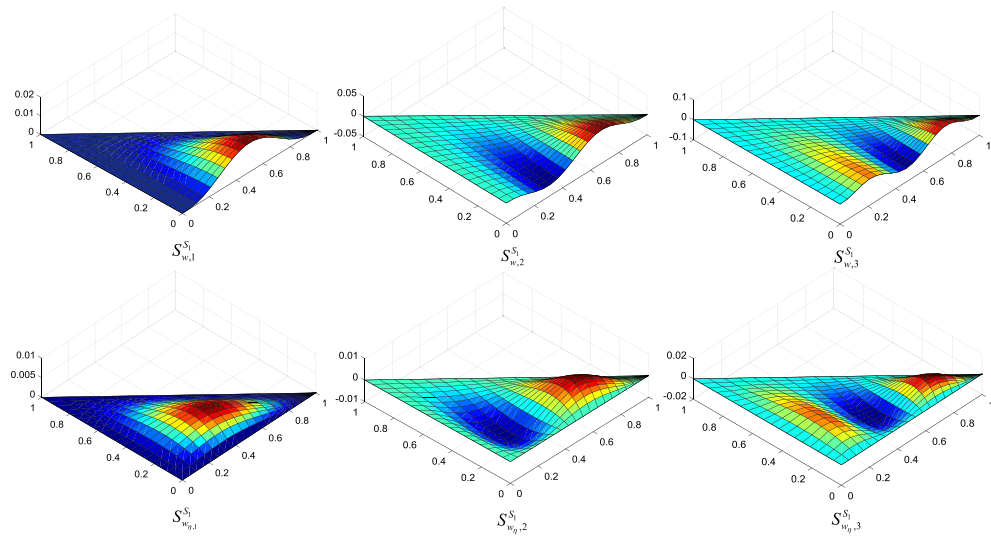


FIGURE 12 Edge functions for a unit triangular element on side 1

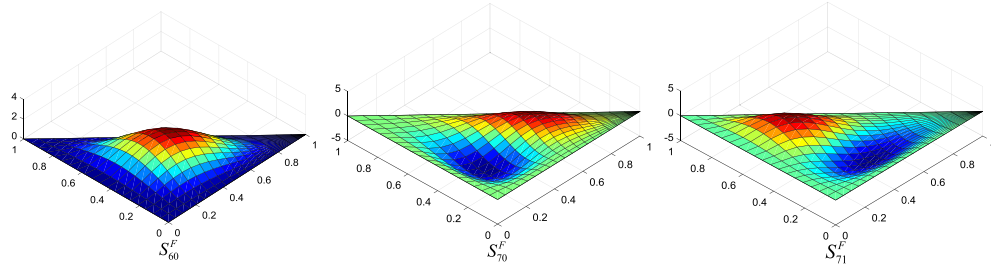


FIGURE 13 First three face functions for a unit triangular element

functions are expressed as

$$\begin{aligned} S_{60}^F &= C_{60}\xi^2\eta^2(1-\xi-\eta)^2 \\ S_{70}^F &= C_{70}5\xi^2\eta^2(1-\xi-\eta)^2(2\xi+\eta-1) \\ S_{71}^F &= C_{71}5\xi^2\eta^2(1-\xi-\eta)^2(3\eta-1). \end{aligned} \quad (46)$$

They are plotted in Figure 13. Both the function values and the normal derivatives of the bases vanish on the boundaries. Appendix summarizes all the hierarchical bases for triangular elements.

5 | NUMERICAL IMPLEMENTATION

5.1 | Basis transformation

The hierarchical bases that are developed above using Jacobi polynomials can be calculated efficiently via the recursion formulas in Equations (25) and (26). However, since they are defined in natural coordinates, they cannot be directly applied to elements that have curved boundaries because of the difficulties of satisfying the C^1 conformity. To overcome this problem, a basis transformation is invoked to transform them into nodal bases. For a quadrilateral element, as shown in Figure 14A, the displacement field, namely, w , on the unit square domain can be approximated by the hierarchical bases as

$$w(\xi, \eta) = \mathbf{N}^T \mathbf{a}, \quad (47)$$

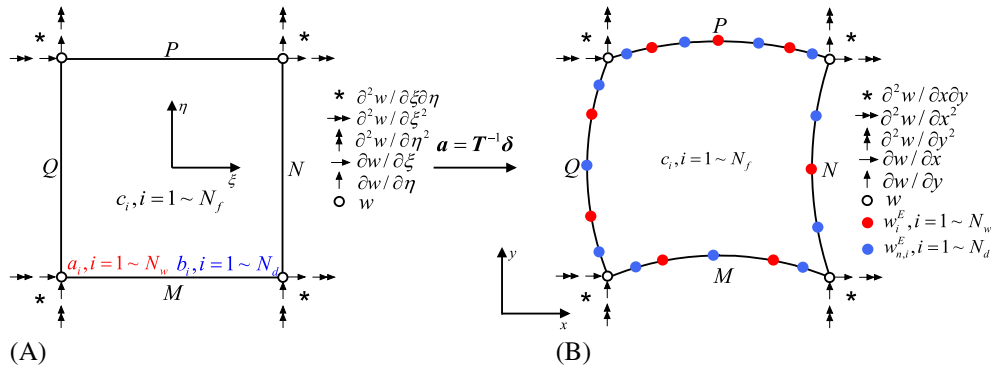


FIGURE 14 Basis transformation for quadrilateral elements. A, Coefficients of hierarchical bases; B, Variables of nodal bases. Here, $M = 2$, $N = 1$, $P = 3$, $Q = 2$, and $\Delta = 1$

where \mathbf{N} is a vector of the hierarchical bases and \mathbf{a} is the generalized displacement vector, which are expressed as

$$\begin{aligned}\mathbf{N}^T &= \left[S_w^{V_1}, \dots, S_{w,\xi\eta}^{V_1}, \dots, \dots, S_w^{V_4}, \dots, S_{w,\xi\eta}^{V_4}, S_{w,1}^{S_1}, \dots, S_{w,M}^{S_1}, \dots, \dots, S_{w,1}^{S_4}, \dots, S_{w,Q}^{S_4} \right. \\ &\quad \left. S_{w_n,1}^{S_1}, \dots, S_{w_n,M+\Delta}^{S_1}, \dots, \dots, S_{w_n,1}^{S_4}, \dots, S_{w_n,Q+\Delta}^{S_4}, S_{11}^F, \dots, S_{H_\xi H_\eta}^F \right] \\ \mathbf{a}^T &= \left[w^{V_1}, \dots, w_{\xi\eta}^{V_1}, \dots, \dots, w^{V_4}, \dots, w_{\xi\eta}^{V_4}, a_1, \dots, a_{N_w}, b_1, \dots, b_{N_d}, c_1, \dots, c_{N_f} \right],\end{aligned}\quad (48)$$

where M , N , P , and Q are the numbers of edge functions for w , V_i ($i = 1, 2, 3, 4$) denotes vertex i , and S_i ($i = 1, 2, 3, 4$) denotes side i . The numbers of edge functions for normal derivatives w_n on each side are set as $M + \Delta$, $N + \Delta$, $P + \Delta$, and $Q + \Delta$, respectively. The increment Δ is typically set to 1 for straight-sided elements to ensure the C^1 conformity. However, more nodes can be used to improve the interpolation accuracy of normal derivatives (namely, the C^1 conformity) in elements that have curved boundaries. Accordingly, the total number of edge functions is $N_w = M + N + P + Q$ for w and $N_d = M + N + P + Q + 4\Delta$ for w_n , whereas the number of face functions is $N_f = H_\xi H_\eta$.

Using proper mapping functions, the unit domain in Figure 14A can be mapped into a curved domain in global coordinates, as shown in Figure 14B. In this work, the C^0 blending functions^{1,35} are employed as the exact mapping functions for our quadrilateral and triangular elements. The transformed nodal variables are also expressed in Figure 14B. The vertex unknowns in natural coordinates have been transformed into variables with respect to global coordinates. The nodal variables, namely, w and w_n (deflection and normal derivative), are also allocated on each edge in x - y coordinates, and the numbers of these variables are the same as those of the hierarchical edge functions for w and w_n . By evaluating the nodal values of Equation (47), one can obtain the following relation:

$$\boldsymbol{\delta} = \mathbf{T}\mathbf{a}, \quad (49)$$

where $\boldsymbol{\delta}$ contains all the transformed nodal variables and the unchanged coefficients c_i that are attached to the face functions and \mathbf{T} is the transition matrix. Consequently, the displacement field can be rewritten as

$$w(\xi, \eta) = \mathbf{N}^T \mathbf{T}^{-1} \boldsymbol{\delta} = \tilde{\mathbf{N}}^T \boldsymbol{\delta}, \quad (50)$$

where $\tilde{\mathbf{N}}$ contains the interpolative nodal bases and the face functions. Similarly, the basis transformation for triangular elements is illustrated in Figure 15. Due to the collocation property of $\tilde{\mathbf{N}}$, the element assembly and boundary condition imposition can be easily performed via the FEM, which is the typically used approach. Moreover, the C^1 conformity of these elements is exactly satisfied in parallelograms and straight-sided triangular elements since the Jacobian is constant. For elements that have curved boundaries, only the C^0 continuity of field variable w is exactly satisfied; the continuity of the normal derivative is satisfied on the nodes. In this case, these elements are referred to as *quasi-conforming* elements in this work. However, as will be shown, fast convergence can still be realized by using GL points as the nodes for w_n .

5.2 | Node collocation

In conventional h -version Lagrange elements, equally spaced (ES) nodes are widely used in elements of moderately high order. For example, three and four nodes are used on each edge of quadratic and cubic elements. However, for p -version

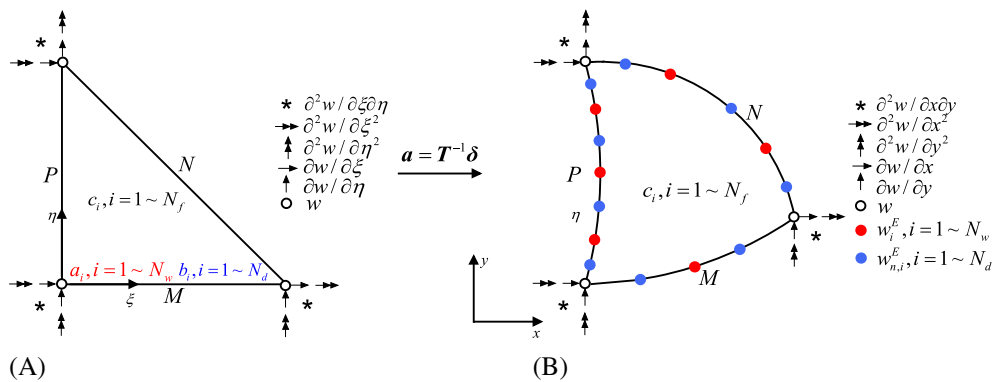


FIGURE 15 Basis transformation for triangular elements. A, Coefficients of hierarchical bases; B, Variables of nodal bases. Here, $M = 1$, $N = 2$, $P = 3$, and $\Delta = 1$

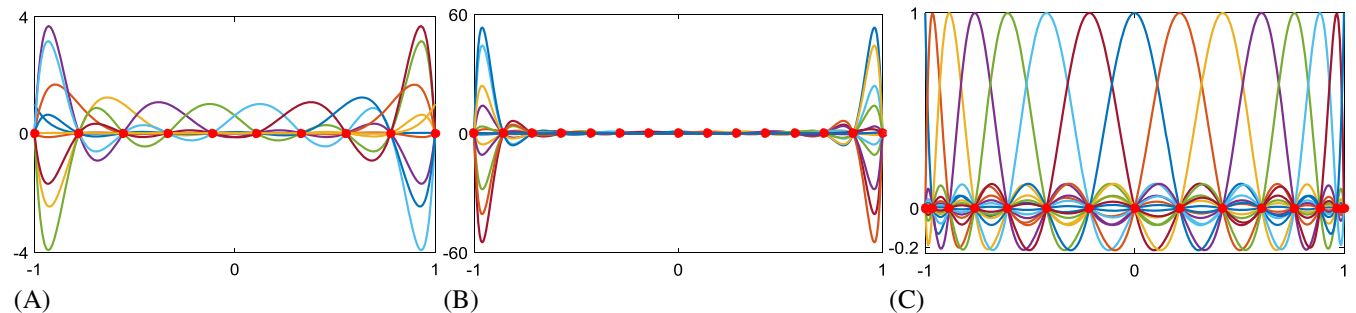


FIGURE 16 Comparison of Lagrange bases that were obtained by various nodes. A, 10 equally spaced nodes; B, 15 equally spaced nodes; C, 15 Gauss-Lobatto nodes

approximation, more nodes may be required on element boundaries when the element order is high. In such cases, ES nodes often result in poorly conditioned matrices because of the significant numerical oscillations when many nodes are used (see Figure 16A,B). Therefore, hierarchical bases that are based on orthogonal polynomials are widely used in p -version finite elements.³⁶ However, this may also render inconvenience in the imposition of nonhomogeneous boundary conditions and element assembly. To solve this problem, inspired by the DQM,³⁷ Liu et al^{38,39} developed a p -version finite element in which Lagrange functions that were based on GL quadrature points were used as the edge functions. Via this approach, the numerical oscillations were eliminated, whereas boundary condition imposition and element assembly could be easily performed. Figure 16C shows the Lagrange bases that are based on GL nodes. Each basis attains its maximum value on the corresponding node, and the function value varies over a small range of approximately $[-0.2, 1]$. In addition, this range is independent of the number of nodes; hence, very high-order approximation is possible using these bases.⁴⁰ For more information about Lagrange node collocation on surfaces and bodies, please refer to other works.⁴¹⁻⁴³ In the present work, since the transformed bases (in natural coordinates) for w and w_n on element boundaries are the one-dimensional C^2 and C^1 Hermite bases (see Figure 17), respectively, the optimized nodes that have small numerical oscillations are no longer GL nodes. However, they can be derived via a similar approach by letting each basis reach its maximum value at the attached node. In the following, we will derive the optimized nodes for C^1 Hermite bases as an example.

As illustrated in Figure 18, consider a one-dimensional function, namely, $f(\xi)$, that is defined in $[-1, 1]$ with values on nodes $[\xi_1 = -1, \xi_2, \dots, \xi_{N-1}, \xi_N = 1]$ and first-order derivatives at two ends. The C^1 Hermite interpolation of f can be expressed as

$$\tilde{f}(\xi) = h_1^{(1)}(\xi) f'(-1) + h_N^{(1)}(\xi) f'(1) + \sum_{i=1}^N h_i(\xi) f(\xi_i), \quad (51)$$

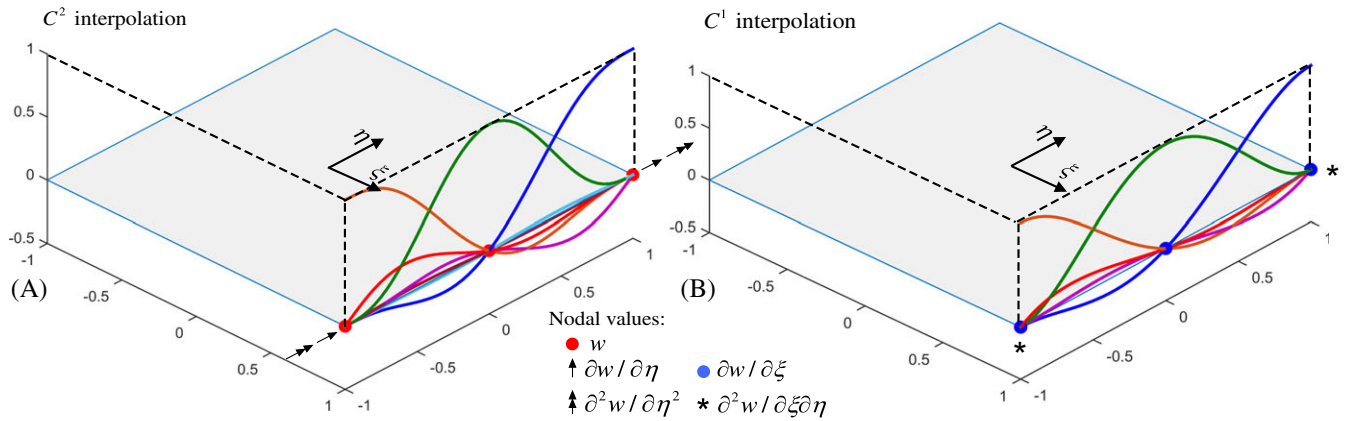


FIGURE 17 Transformed bases on an element boundary (side 2) with three nodes. A, C^2 Hermite bases for w ; B, C^1 Hermite bases for $\partial w / \partial \xi$

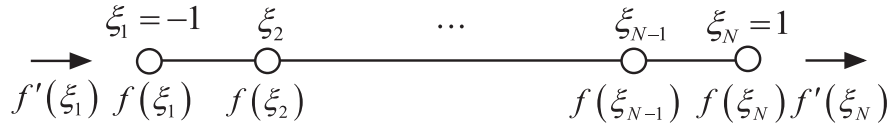


FIGURE 18 C^1 Hermite interpolation with N nodes

where $h_1^{(1)}(\xi)$ and $h_N^{(1)}(\xi)$ are the bases that are related to the derivatives and $h_i(\xi)$ are the bases that are attached to the function values on node ξ_i . They are defined as

$$\begin{aligned} h_1^{(1)}(\xi) &= \frac{1 - \xi^2}{2} L_1(\xi); & h_N^{(1)}(\xi) &= \frac{\xi^2 - 1}{2} L_N(\xi) \\ h_1(\xi) &= (c_1\xi + c_2) \frac{1 - \xi}{2} L_1(\xi); & h_i(\xi) &= \frac{1 - \xi^2}{1 - \xi_i^2} L_i(\xi), j = 2 \sim N - 1; & h_N(\xi) &= (c_3\xi + c_4) \frac{1 + \xi}{2} L_N(\xi), \end{aligned} \quad (52)$$

where $L_i(\xi), i = 1, 2, \dots, N$ are the Lagrange functions, which are defined as

$$L_i(\xi) = \prod_{k=1, k \neq i}^N \frac{\xi - \xi_k}{\xi_i - \xi_k}, \quad (53)$$

and the coefficients $c_i, i = 1, 2, 3, 4$, which are expressed as

$$c_1 = \frac{1}{2} - L'_1(\xi_1), \quad c_2 = \frac{3}{2} - L'_1(\xi_1); \quad c_3 = -\frac{1}{2} - L'_N(\xi_N), \quad c_4 = \frac{3}{2} + L'_N(\xi_N), \quad (54)$$

and can be determined from the interpolation requirements

$$h_1(-1) = 1; \quad h'_1(-1) = 0; \quad h_N(1) = 1; \quad h'_N(1) = 0. \quad (55)$$

The Hermite bases that are attached to the middle nodes have the following properties:

$$h_i(\xi_j) = \delta_{ij} \quad \text{and} \quad h'_i(\pm 1) = 0, \quad i = 2, 3, \dots, N - 1. \quad (56)$$

To obtain the optimized nodes, we force the middle bases, namely, $h_i(\xi), i = 2, 3, \dots, N - 1$, to attain their maximum values at nodes ξ_i as the Lagrange bases that are based on GL nodes, which results in the following equations:

$$g_i(\xi) = \frac{dh_i(\xi_i)}{d\xi} = \frac{2\xi_i}{\xi_i^2 - 1} + \frac{dL_i(\xi_i)}{d\xi} = 0; \quad \xi = [\xi_2, \dots, \xi_{N-1}] \quad i = 2, 3, \dots, N - 1. \quad (57)$$

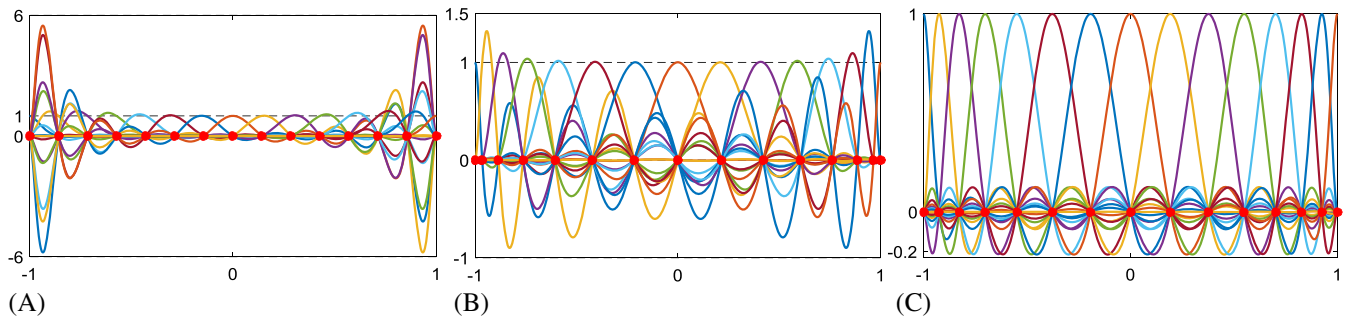


FIGURE 19 Comparison of C^1 Hermite bases that were obtained by various different nodes. A, 15 equally spaced nodes; B, 15 Gauss-Lobatto nodes; C, 15 Gauss-Jacobi (3, 3) nodes

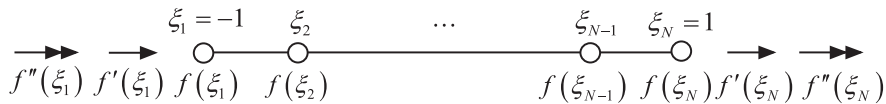


FIGURE 20 C^2 Hermite interpolation with N nodes

The $N - 2$ middle nodes can be determined from the system of $N - 2$ nonlinear equations. The Newton-Raphson method can be used to solve these equations efficiently, and the required Jacobian matrix can be computed from

$$\frac{\partial g_i(\xi)}{\partial \xi_j} = \begin{cases} -\frac{2(1+\xi_j^2)}{(1-\xi_j^2)^2} - \sum_{k=1, k \neq j}^N \frac{1}{(\xi_j - \xi_k)^2}, & (i = j) \\ \frac{1}{(\xi_j - \xi_i)^2}, & (i \neq j). \end{cases} \quad (58)$$

The GL nodes can be used as the initial guess. The solutions of Equation (57) are the zeros of Jacobi polynomial $J^{(3, 3)}_{N-2}(\xi)$; hence, they are referred to as GJ nodes in this work. Figure 19 compares the C^1 Hermite bases that were obtained by nodes of various types. The numerical oscillations are more profound in bases that use ES nodes than in the bases that are generated by GJ nodes.

Figure 20 illustrates the C^2 Hermite interpolation, where the derivative up to second order at each end should be interpolated (the fifth-order Hermite bases in Equation (20) correspond to the special case of $N = 2$). The derivation of the optimized C^2 GJ nodes is similar to the derivation above. They are the zeros of Jacobi polynomial $J^{(5, 5)}_{N-2}(\xi)$.

5.3 | FEM discretization

For the isotropic Kirchhoff plates that are considered in this work, the potential functional and maximum kinetic energy are expressed as

$$\begin{aligned} \Pi &= \frac{D}{2} \iint_{\Omega} \left(\frac{\partial^2 w}{\partial x^2} \right)^2 + \left(\frac{\partial^2 w}{\partial y^2} \right)^2 + 2v \frac{\partial^2 w}{\partial x^2} \frac{\partial^2 w}{\partial y^2} + 2(1-v) \left(\frac{\partial^2 w}{\partial x \partial y} \right)^2 dx dy - \iint_{\Omega} q w dx dy \\ T_{\max} &= \iint_{\Omega} \frac{1}{2} \rho h \omega^2 w^2 dx dy, \end{aligned} \quad (59)$$

where v is Poisson's ratio, $D = Eh^3/12(1-v^2)$ is the flexural rigidity, ρ is the volume density, h is the thickness, and ω is the angular frequency. For numerical discretization, we define the following weighting matrices for differentiation as the differential quadrature method:

$$\mathbf{D}_0 = \begin{bmatrix} \mathbf{N}^T(\xi_1, \eta_1) \\ \vdots \\ \mathbf{N}^T(\xi_{N_\xi}, \eta_{N_\eta}) \end{bmatrix}, \quad \mathbf{D}_{xx} = \begin{bmatrix} \mathbf{N}''_{,xx}^T(\xi_1, \eta_1) \\ \vdots \\ \mathbf{N}''_{,xx}^T(\xi_{N_\xi}, \eta_{N_\eta}) \end{bmatrix}, \quad \mathbf{D}_{yy} = \begin{bmatrix} \mathbf{N}''_{,yy}^T(\xi_1, \eta_1) \\ \vdots \\ \mathbf{N}''_{,yy}^T(\xi_{N_\xi}, \eta_{N_\eta}) \end{bmatrix}, \quad \mathbf{D}_{xy} = \begin{bmatrix} \mathbf{N}''_{,xy}^T(\xi_1, \eta_1) \\ \vdots \\ \mathbf{N}''_{,xy}^T(\xi_{N_\xi}, \eta_{N_\eta}) \end{bmatrix}, \quad (60)$$

where (ξ_i, η_j) are the GL quadrature points³⁹ and N_ξ and N_η are the numbers of quadrature points in the two directions. The following chain rules of differentiation are needed in the computation of Equation (60):

$$\begin{bmatrix} \frac{\partial w}{\partial x} \\ \frac{\partial w}{\partial y} \end{bmatrix} = \frac{1}{|\mathbf{J}|} \begin{bmatrix} J_{22} & -J_{12} \\ -J_{21} & J_{11} \end{bmatrix} \begin{bmatrix} \frac{\partial w}{\partial \xi} \\ \frac{\partial w}{\partial \eta} \end{bmatrix} \quad (61)$$

$$\begin{bmatrix} \frac{\partial^2 w}{\partial x^2} \\ \frac{\partial^2 w}{\partial y^2} \\ \frac{\partial^2 w}{\partial x \partial y} \end{bmatrix} = \frac{1}{|\mathbf{J}|^2} \begin{bmatrix} J_{22}^2 & J_{12}^2 & -2J_{12}J_{22} \\ J_{21}^2 & J_{11}^2 & -2J_{11}J_{21} \\ -J_{21}J_{22} & -J_{11}J_{12} & J_{11}J_{22} + J_{12}J_{21} \end{bmatrix} \begin{bmatrix} \frac{\partial^2 w}{\partial \xi^2} - \frac{\partial w}{\partial x} \frac{\partial^2 x}{\partial \xi^2} - \frac{\partial w}{\partial y} \frac{\partial^2 y}{\partial \xi^2} \\ \frac{\partial^2 w}{\partial \eta^2} - \frac{\partial w}{\partial x} \frac{\partial^2 x}{\partial \eta^2} - \frac{\partial w}{\partial y} \frac{\partial^2 y}{\partial \eta^2} \\ \frac{\partial^2 w}{\partial \eta \partial \xi} - \frac{\partial w}{\partial x} \frac{\partial^2 x}{\partial \eta \partial \xi} - \frac{\partial w}{\partial y} \frac{\partial^2 y}{\partial \eta \partial \xi} \end{bmatrix}, \quad (62)$$

where $x(\xi, \eta)$ and $y(\xi, \eta)$ are the geometry mapping functions and \mathbf{J} is the Jacobian matrix, which is defined as

$$\mathbf{J} = \begin{bmatrix} J_{11} & J_{12} \\ J_{21} & J_{22} \end{bmatrix} = \begin{bmatrix} \frac{\partial x}{\partial \xi} & \frac{\partial y}{\partial \xi} \\ \frac{\partial x}{\partial \eta} & \frac{\partial y}{\partial \eta} \end{bmatrix}. \quad (63)$$

Using Equations (50) and (60), the functional in Equation (59) can be discretized as

$$\begin{aligned} \Pi &= \frac{1}{2} \boldsymbol{\delta}^T \mathbf{T}^{-T} \mathbf{H}^T \mathbf{B} \mathbf{H} \mathbf{T}^{-1} \boldsymbol{\delta} - \mathbf{q}^T \mathbf{C} \mathbf{D}_0 \mathbf{T}^{-1} \boldsymbol{\delta} \\ T_{\max} &= \frac{1}{2} \omega^2 \rho h \boldsymbol{\delta}^T \mathbf{T}^{-T} \mathbf{D}_0^T \mathbf{C} \mathbf{D}_0 \mathbf{T}^{-1} \boldsymbol{\delta}, \end{aligned} \quad (64)$$

where

$$\begin{aligned} \mathbf{B} &= D \begin{bmatrix} \mathbf{C} & v\mathbf{C} & \mathbf{0} \\ v\mathbf{C} & \mathbf{C} & \mathbf{0} \\ \mathbf{0} & \mathbf{0} & 2(1-v)\mathbf{C} \end{bmatrix}, \quad \mathbf{H} = \begin{bmatrix} \mathbf{D}_{xx} \\ \mathbf{D}_{yy} \\ \mathbf{D}_{xy} \end{bmatrix}, \quad \mathbf{q} = [q(\xi_1, \eta_1), \dots, q(\xi_{N_\xi}, \eta_{N_\eta})]^T \\ \mathbf{C} &= \text{diag} \left\{ J_{ij} C_i^\xi C_j^\eta \right\}, \quad J_{ij} = |\mathbf{J}(\xi_i, \eta_j)|, \end{aligned} \quad (65)$$

in which C_i^ξ and C_j^η are the quadrature weightings and J_{ij} are the values of the Jacobian at quadrature points. Finally, the stiffness and mass matrices and load vector can be expressed as

$$\begin{aligned} \mathbf{K} &= \mathbf{D} \mathbf{T}^{-T} [\mathbf{D}_{xx}^T \mathbf{C} \mathbf{D}_{xx} + \mathbf{D}_{yy}^T \mathbf{C} \mathbf{D}_{yy} + v (\mathbf{D}_{xx}^T \mathbf{C} \mathbf{D}_{yy} + \mathbf{D}_{yy}^T \mathbf{C} \mathbf{D}_{yy}) + 2(1-v) \mathbf{D}_{xy}^T \mathbf{C} \mathbf{D}_{xy}] \mathbf{T}^{-1} \\ \mathbf{M} &= \rho h \mathbf{T}^{-T} \mathbf{D}_0^T \mathbf{C} \mathbf{D}_0 \mathbf{T}^{-1}, \quad \mathbf{F} = \mathbf{T}^{-T} \mathbf{D}_0^T \mathbf{C} \mathbf{q}. \end{aligned} \quad (66)$$

The boundary condition imposition of present elements can be found in the early literature by Cowper et al⁴⁴ and, more recently, by Ivannikov et al⁴⁵; hence, it is omitted in this work due to space limitations.

6 | RESULTS AND DISCUSSION

In this section, numerical examples for vibration and deformation analyses of Kirchhoff plates will be presented for evaluating the computational performance of these quadrilateral (abbreviated as *Quad.*) and triangular (*Tri.*) elements. First, the complete order and the computational efficiency of the elements are analyzed. Then, the computational performance of fully C^1 conforming elements (straight-sided triangles and parallelograms) is evaluated via bending and free vibration analyses of thin plates. A singular problem is employed to demonstrate the advantages of these elements in local p -refinement. The performance of elements that have curved boundaries is studied in the third part.

6.1 | Complete element order and computational efficiency

For simplicity, unless otherwise stated, all the numbers of middle-side nodes have the same values of $N \geq 0$ for w and $N+1$ for w_n in this work, whereas the numbers of face functions are set as $N_f = H_\xi H_\eta = (N+1)^2$ for quadrilateral elements and $N_f = (N+1)N/2$ for triangular elements. Therefore, for a specified value of N , there are $N^2 + 10N + 29$ bases for a quadrilateral element and $(N+6)(N+7)/2$ bases for a triangular element.

The edge and vertex bases in this work are constructed via the blending function method instead of tensor-product one-dimensional bases for local p -refinement. The projection test is used to analyze the complete order of the elements, and the results are shown in Figure 21. The complete order of both quadrilateral and triangular elements is $N+5$. Incomplete high-order monomials, along with two additional polynomials, are included in the quadrilateral elements. However,

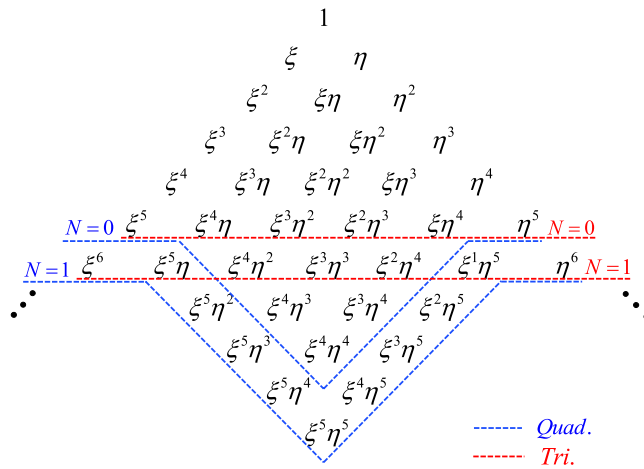


FIGURE 21 Complete order of the quadrilateral and triangular elements

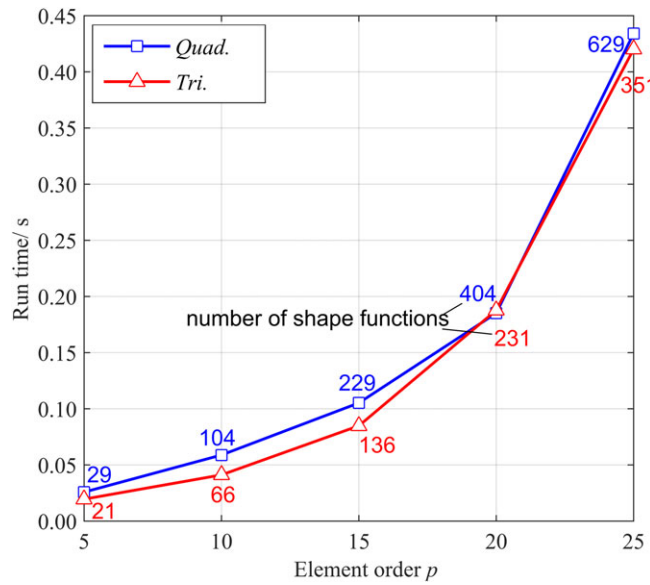


FIGURE 22 Run time of stiffness matrix generation versus complete order p [Colour figure can be viewed at wileyonlinelibrary.com]

these incomplete terms do not appear in our triangular elements. Although the number of nodes, namely, N , is set as 0 and 1 in the figure, the regularity of the complete order can be extended to any value of N .

In the p -version FEM, computational costs are mainly incurred in the generation of element matrices, especially when the element order is very high. To evaluate the computational efficiency of these elements, Figure 22 presents the run time for the generation of stiffness matrices of present quadrilateral and triangular elements at various values of complete order p . The total number of shape functions for each p is also specified in the figure. The number of quadrature points is set as $p \times p$ for each case. The MATLAB codes were run on a personal computer with Core i5 4200 U @ 1.60-GHz CPU. The computation process includes the calculation of the high-order bases and their up-to-second-order derivatives, the computation of the up-to-second-order Jacobian, the transformation in Equation (50), and the linear summation of the GL quadrature. The run time for both types of elements is less than half a second, even when $p = 25$.

6.2 | Analysis using conforming elements

As discussed previously, if the elements are parallelograms or straight-sided triangles, the C^1 continuity can be exactly satisfied. In this section, the computational performance of these conforming elements will be studied. The developed GJ points are used as the nodes for w and w_n on element boundaries to improve the numerical performance.

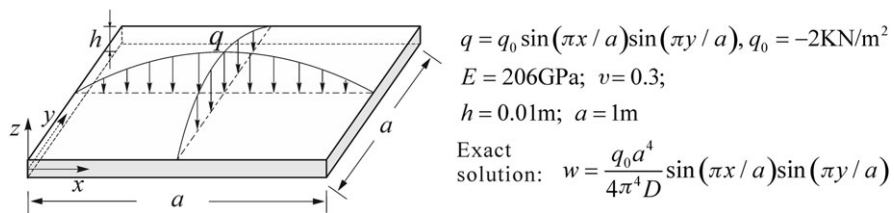


FIGURE 23 Simply supported square plate under a sinusoidal load

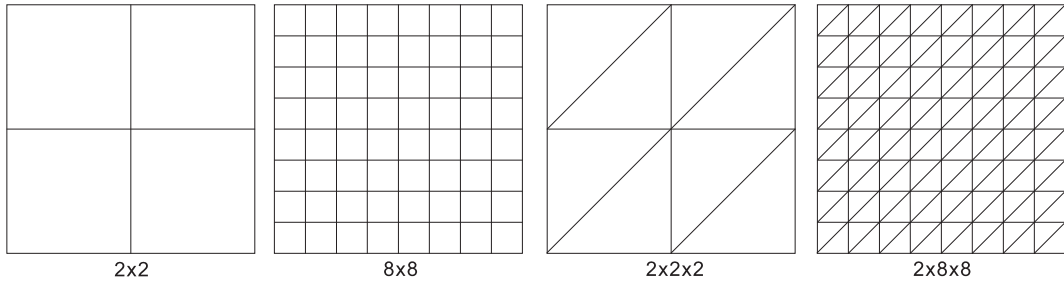


FIGURE 24 Nondistorted meshes for h -refinement

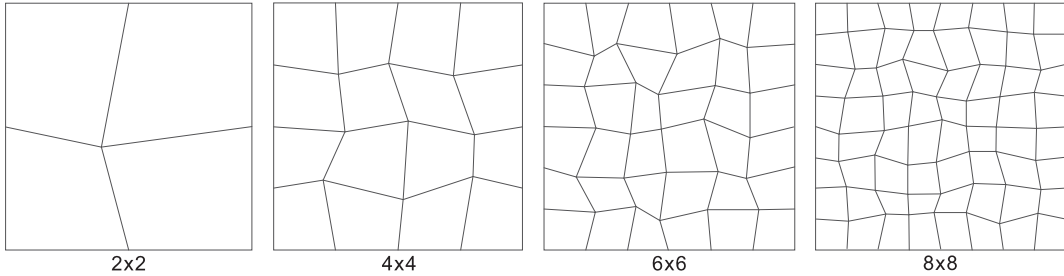


FIGURE 25 Distorted quadrilateral meshes for h -refinement

6.2.1 | Bending of a square plate

The first example, which is illustrated in Figure 23, is a simply supported square plate that is under a sinusoidally distributed load. Both h - and p -refinements will be performed in the analyses. Figure 24 shows the coarsest and finest meshes for h -refinement using nondistorted quadrilateral and triangular elements. Distorted quadrilateral and triangular meshes for h -refinement are shown in Figures 25 and 26, respectively, whereas the meshes for p -refinement are shown in Figure 27. The quadrilateral elements in h -refinement are generated by forcing the numbers of nodes to satisfy $M = N = P = Q = N_f = 0$; these elements are the same as Watkins' 28-DOF conforming rectangular elements. The triangular elements in h -refinement are generated by forcing the numbers of nodes to satisfy $M = N = P = N_f = 0$; they are the same as the TUBA-21 elements. The distorted quadrilateral elements in Figure 25 are indeed nonconforming; they are studied here to demonstrate the influence of C^1 conformity on the convergence rate. Nevertheless, our p -version distorted quadrilateral elements perform very well, as shown in the next part. The energy norm of the displacement error¹ and the

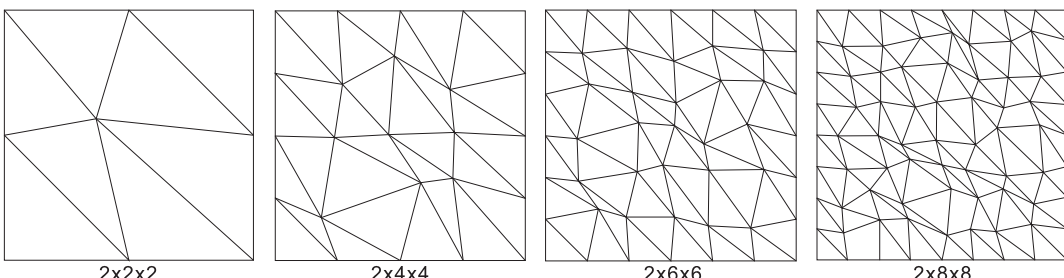


FIGURE 26 Distorted triangular meshes for h -refinement

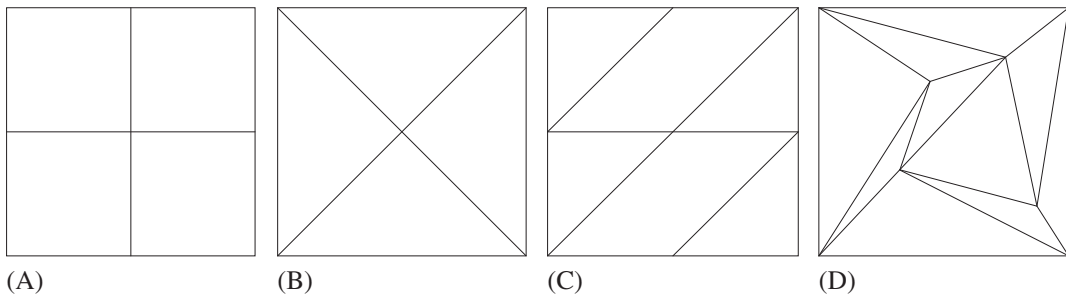


FIGURE 27 Meshes for p -refinement. A, Quad. mesh; B, Tri. mesh; C, Combinational mesh; D, Distorted Tri. mesh

relative error of the central-point moment M_x , which are defined as follows, will be used to study the convergence rate:

$$\|e\|_E = \left[D \iint_{\Omega} \left(\frac{\partial^2 e}{\partial x^2} \right)^2 + \left(\frac{\partial^2 e}{\partial y^2} \right)^2 + 2v \frac{\partial^2 e}{\partial x^2} \frac{\partial^2 e}{\partial y^2} + 2(1-v) \left(\frac{\partial^2 e}{\partial x \partial y} \right)^2 dx dy \right]^{1/2} \quad (67)$$

$$\|e_r\|_{M_x} = \frac{|M_{x,app} - M_{x,Exact}|}{M_{x,Exact}}, \quad M_x = -D \left(\frac{\partial^2 w}{\partial x^2} + v \frac{\partial^2 w}{\partial y^2} \right), \quad (68)$$

where $e = w^* - w_{app}$ is the difference between the exact solution, namely, w^* , and the approximated numerical solution, namely, w_{app} ; $M_{x,app}$ is the approximated numerical solution of moment M_x ; and $M_{x,Exact}$ denotes the exact solution.

The errors are presented in logarithmic scale in Figure 28, where N is set as 0, 2, 4, 6, 8 for the p -refinement in Figure 27A,C,D and as 1, 3, 5, 7, 9 in Figure 27B so that the numbers of DOFs are similar for comparison. According to Figure 28A, the convergence rate of the nondistorted quadrilateral elements in h -refinement is higher than that of the nondistorted triangular elements. This is because the number of triangular elements is higher than the number of quadrilateral elements if the numbers of DOFs of the two types of elements are the same. As a result, the global continuity of the solution space of triangular elements is poorer than that of quadrilateral elements. The convergence rate of distorted triangular elements in h -refinement is slightly lower than that of the nondistorted mesh. The convergence of distorted quadrilateral elements in h -refinement is poor due to the loss of C^1 conformity, which is a common problem in the h -version FEM. Exponential rates of convergence are observed in all cases of p -refinement. The convergence rate of nondistorted triangular elements in p -refinement is higher than that of nondistorted quadrilateral elements because the complete order of triangular elements is higher than that of quadrilateral elements when the same number of DOFs is

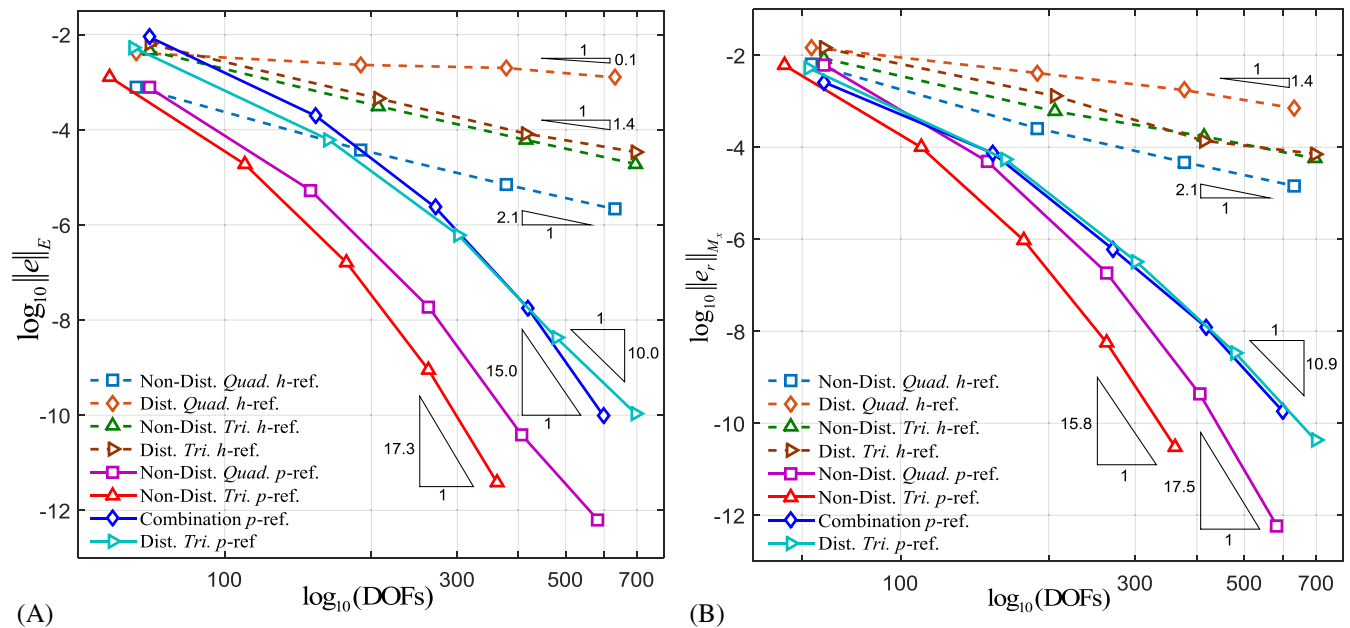


FIGURE 28 Convergence rate comparison. A, Error in the energy norm; B, Relative error in the logarithm of central-point moment M_x . DOFs, degrees of freedom

used (Figure 21). The convergence rate of the combinational case is lower compared to the cases with a single type of elements. This phenomenon is expected because the global continuity in the mesh (Figure 27C) is worse than in the other cases due to the use of more elements. However, fast convergence is also realized when more DOFs are used. Satisfactory performance can still be realized when distorted triangular elements are used. The convergence rate is very close to that of the combinational mesh in which the element distortion is less severe. Fast convergence of the central-point moment is also observed in Figure 28B.

6.2.2 | Plate with a singularity

In the second example, a fully simply supported L-shaped plate under a uniformly distributed flexural load of $q = -1000 \text{ N/m}^2$ is employed to study the performance of these elements in local p -refinement. The moment is singular at the inner corner. The dimensions of the plate are specified in Figure 29A. The material constants are taken as $E = 206 \text{ GPa}$ and $\nu = 0.3$, and the thickness is taken as $h = 0.01 \text{ m}$. This example was also used in the work of Ferreira and Bittencourt,²¹ where uniform p -refinement using elements with the same order at each step was considered. To assess the convergence rate, the relative error of the energy norm, which is defined as follows, is used for comparison²¹:

$$E_r = \frac{|U_r - U_i|}{U_r} \times 100\%, \quad (69)$$

where U_r is the energy norm of the reference solution and U_i is the energy norm that is obtained via refinement strategies of various types. The reference solution, namely, U_r , is obtained by using the 28-DOF conforming rectangular elements with a very fine-graded mesh, as shown in Figure 29A, where 15 094 DOFs are used (the results are close to the solutions that were obtained by the 28-DOF elements using a uniform mesh with nearly 100 000 DOFs).

In Figure 29B,C, high-order elements with N_1 nodes are used near the singular corner, whereas low-order elements with N_2 nodes are used in the area away from the singular point. Transition elements are employed to connect the two

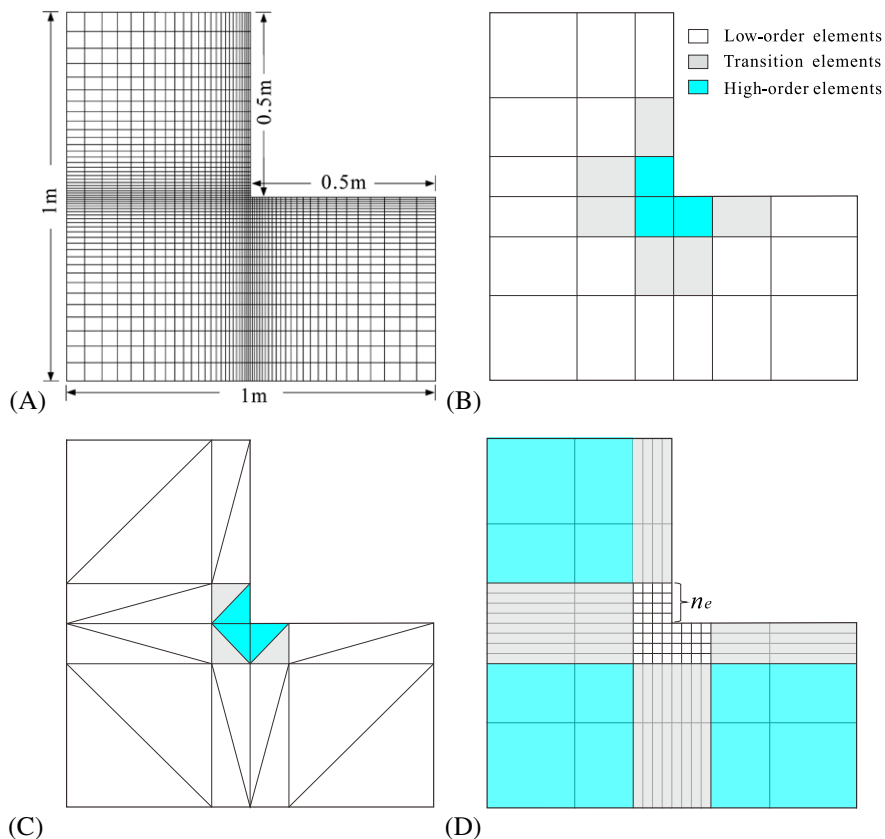


FIGURE 29 L-shaped plate problem. A, Mesh for the reference solution and the dimensions of the plate; B, Local p -refinement with quadrilateral elements; C, Local p -refinement with triangular elements; D, The mesh for local h -refinement

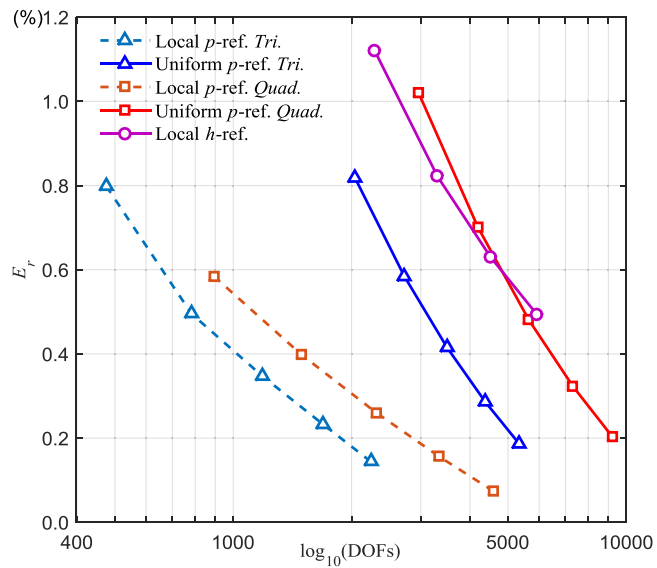


FIGURE 30 Convergence of the relative error of the energy norm, which is expressed as a percentage. DOFs, degrees of freedom

types of elements. For simplicity, the numbers of nodes are set as $N_2 = 0, 2, 4, 6, 8$, and 10 and $N_1 = N_2 + 10$ during the process of local p -refinement. In Figure 30, the results of local p -refinement are compared with the solutions that were obtained via uniform p -refinement with $N = 7, 9, 11, 13$, and 15 in a quadrilateral mesh (Figure 29B) and $N = 9, 11, 13, 15$, and 17 in a triangular mesh (Figure 29C). In both cases, the local p -refinements use fewer DOFs than the uniform p -refinements to achieve the same accuracy. This is because the domain around the singular point contributes mostly to the global energy; thus, more DOFs should be assigned to the singular area.

We have also studied the local h -refinement strategy, which is illustrated in Figure 29D. The mesh profile is similar to that in Figure 29B. However, only mesh refinement with fixed fifth-order elements is used around the singular corner. In the area away from the singular corner, high-order elements with $p = 7$ are used (which realize sufficient accuracy). By setting the number of elements, namely, n_e (see Figure 29D) as $6, 8, 10$, and 12 , we obtain the convergence curve that is shown in Figure 30. The convergence rate of the local h -refinement strategy is close to the rate of the uniform p -refinement strategy using quadrilateral elements. More efficient refinement strategies are possible. This example also demonstrates the potential application of these elements for adaptive analysis.

6.2.3 | Free vibration

In the third example, vibration analysis of a simply supported square plate is employed to study the effects of the node type on the condition numbers of the element matrices and the accuracy of the results. The expression for the natural frequency parameters, which can be found in textbooks, is as follows:

$$\omega_{ij}^* = (i^2 + j^2) (\pi/a)^2 \sqrt{D/\rho h}, \quad (70)$$

where i and j are the wave numbers along each direction, a is the side length, and D , ρ , and h are as defined previously. Six types of nodes are considered here: ES nodes, the GJ nodes that are developed in this work, GL nodes, the first type of Chebyshev nodes, the second type of Chebyshev nodes, and Chebyshev-Gauss-Lobatto nodes. The last four types of non-ES nodes are widely used in DQM; they are defined in the work of Tornabene et al.⁴⁶ Two types of meshes, which are illustrated in Figure 31, are used in the computation. As a measure of accuracy, we define the following relative error, which is expressed in logarithmic form:

$$\log_{10} \|e_r\| = \log_{10} \left| \frac{\omega_{ij} - \omega_{ij}^*}{\omega_{ij}} \right|, \quad (71)$$

where ω_{ij} is the FEM solution and ω_{ij}^* is the exact solution.

Figure 32 shows the normalized errors of the first 10 frequencies that were obtained by these quadrilateral and triangular elements with $p = 10, 20$, and 30 . When $p = 10$, the relative errors of the results that were obtained by the various types of nodes are almost the same. This is because the nodal bases of the nodes of all the types are linearly equivalent, and the

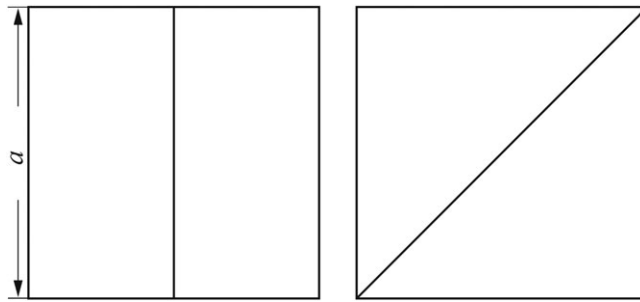


FIGURE 31 Quadrilateral mesh (left) and triangular mesh (right)

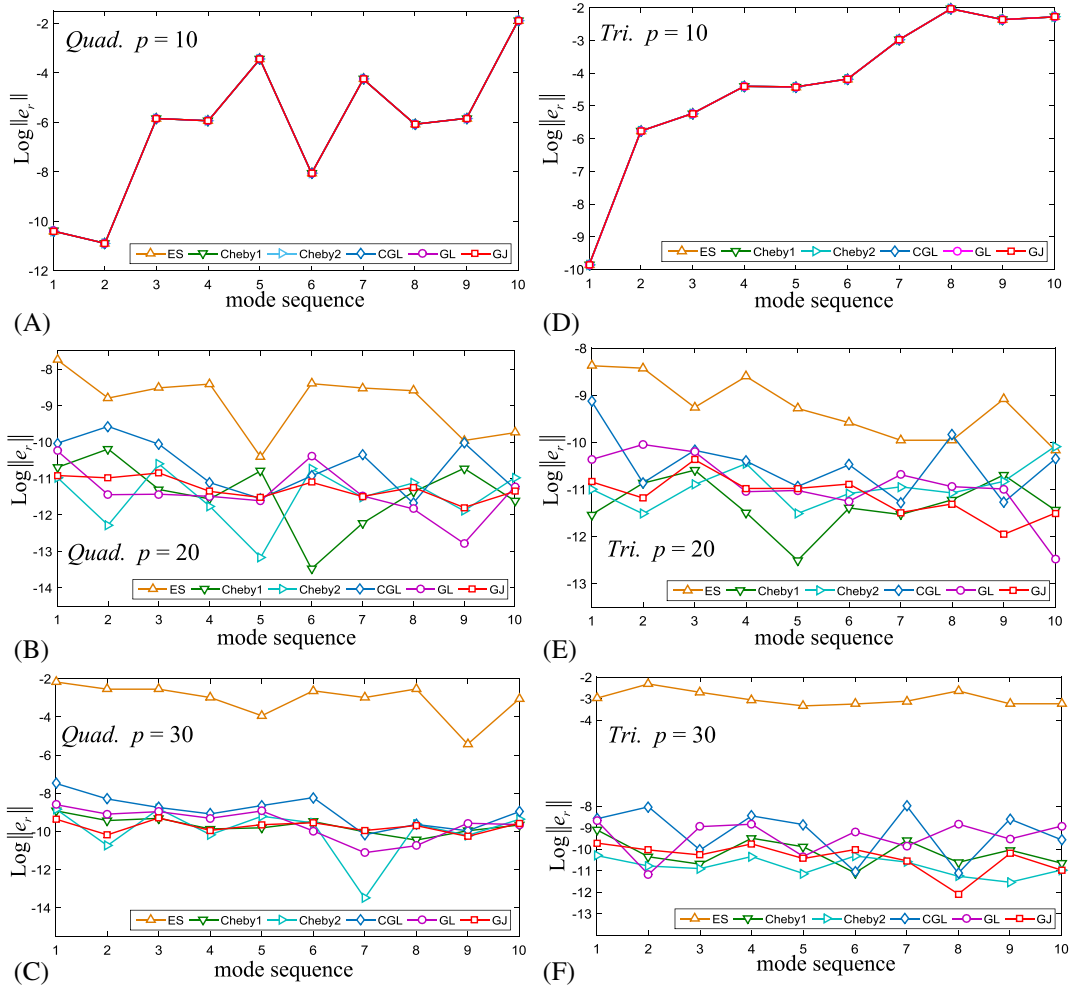


FIGURE 32 Relative errors of the first 10 frequencies with various orders. A, Quad. $p = 10$; B, Quad. $p = 20$; C, Quad. $p = 30$; D, Tri. $p = 10$; E, Tri. $p = 20$; F, Tri. $p = 30$. CGL, Chebyshev-Gauss-Lobatto nodes; Cheby1, the first type of Chebyshev nodes; Cheby2, the second type of Chebyshev nodes; ES, equally spaced nodes; GJ, Gauss-Jacobi nodes; GL, Gauss-Lobatto nodes

corresponding algebraic system is well conditioned. When $p = 20$, more accurate results are obtained using nonuniformly distributed nodes. However, the accuracies of the first two frequencies that were obtained by ES nodes decrease from magnitude 10^{-10} to 10^{-8} . When $p = 30$, the accuracy of the ES nodes decreases dramatically and becomes unacceptable, whereas the results that are obtained using nonuniform nodes are still highly accurate. In Figure 33, the corresponding condition numbers of the element matrices that are generated for the various node types are plotted. The condition numbers of these matrices are high since very high-order bases are used. Nevertheless, the bases can still produce highly accurate results (Figure 32), and the results are stable. Moreover, compared with nodes of other types, the GJ nodes that

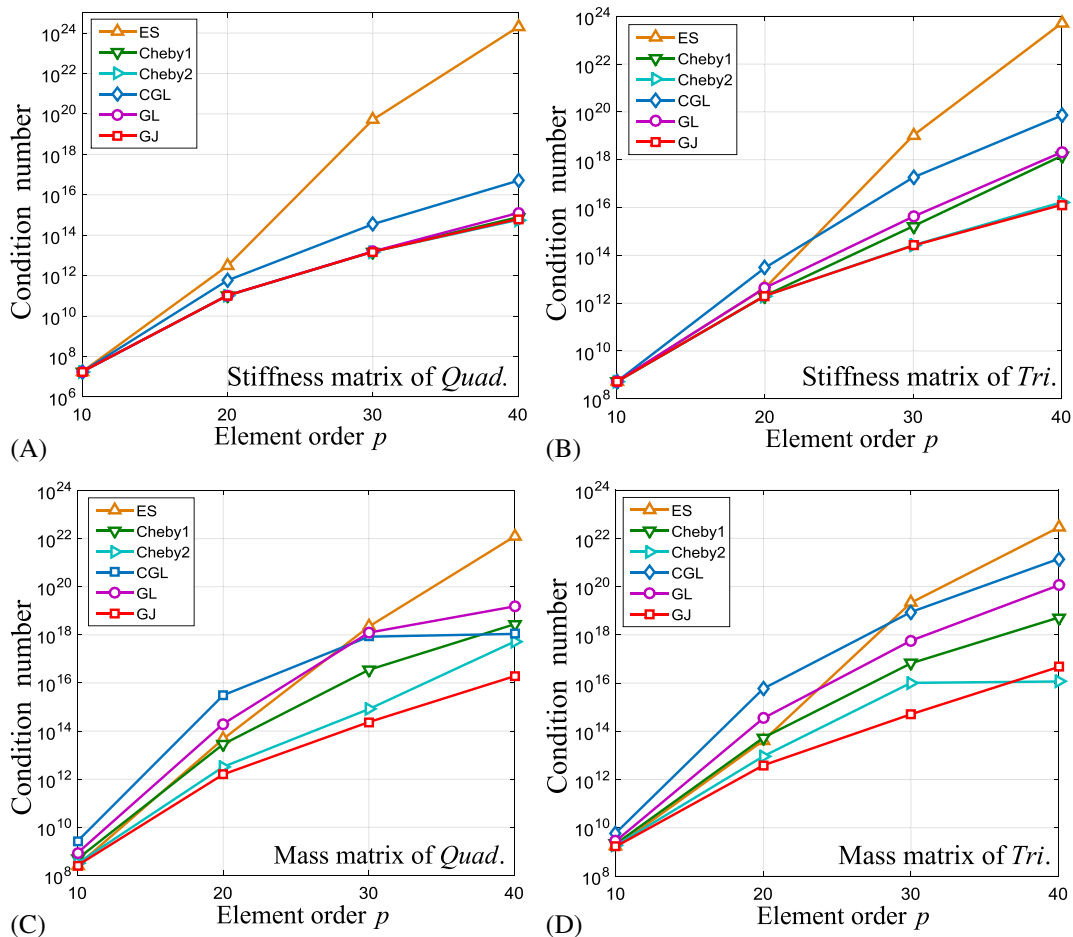


FIGURE 33 Condition numbers of element matrices versus the element order. A, Stiffness matrix of *Quad*; B, Stiffness matrix of *Tri*; C, Mass matrix of *Quad*; D, Mass matrix of *Tri*. CGL, Chebyshev-Gauss-Lobatto nodes; Cheby1, the first type of Chebyshev nodes; Cheby2, the second type of Chebyshev nodes; ES, equally spaced nodes; GJ, Gauss-Jacobi nodes; GL, Gauss-Lobatto nodes

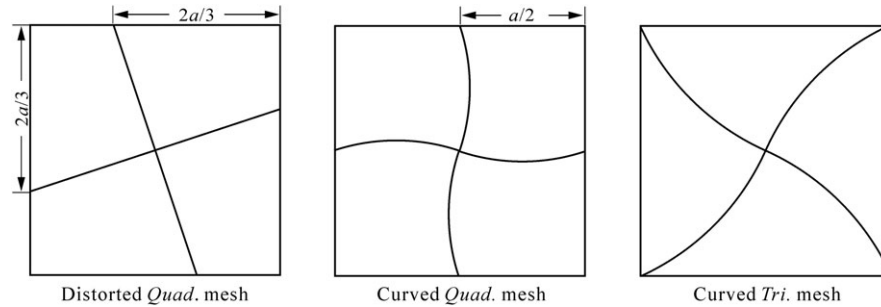


FIGURE 34 Three meshes for the square plate that use quasi-conforming elements

are developed in this work have the lowest condition numbers for all cases, whereas the condition numbers for the ES nodes are the largest.

6.3 | Analysis using quasi-conforming elements

For elements that have curved boundaries (including distorted straight-sided quadrilateral elements), the continuity of the displacement, namely, w , is exactly satisfied on the boundaries, whereas the normal derivative, namely, w_n , is continuous on nodes only. Although C^1 conformity is not fully satisfied, it will be demonstrated in the following that the convergence rate of these elements is still very high. In Section 6.2, the number of nodes of w_n is set as one more than that of w on each

edge. However, as has been discussed in Section 3.2, the number of nodes for w_n can be selected freely because of the inherent characteristics of blending function interpolation. This property is very useful for improving the convergence rate, especially for elements that have curved boundaries. In the following, the number of nodes for w on each edge is denoted by N , whereas the number of nodes for w_n is set as $N + \Delta$. The face function numbers are as previously defined.

6.3.1 | Bending of a square plate

The square plate that was analyzed in Section 5.2 will be considered again in this part with meshes that are generated by elements that have curved boundaries (see Figure 34). The convergence curves of the error energy norm for distorted quadrilateral meshes with $N = 0, 2, 4, 6$, and 8 (p from 5 to 13) are shown in Figure 35A. GL points are used as the nodes for w_n (the nodes for w are still GJ nodes with weights (5, 5)), and Δ ranges from 1 to 3. The results that are obtained by rectangular conforming elements (Figure 27A) are also included in the Figure for comparison. An exponential rate of convergence is observed in all cases with various values of the node-number increment, which is denoted as Δ . Improved convergence rates are obtained when Δ is increased because C^1 continuity is refined as the number of nodes that are used for w_n increases. It is surprising that when $\Delta = 3$, the convergence curve that is obtained by our distorted elements is very close to the results of conforming elements using nondistorted meshes. To examine the influence of the node type on the convergence rate, Figure 35B presents the convergence curves that were obtained by various node types for the distorted

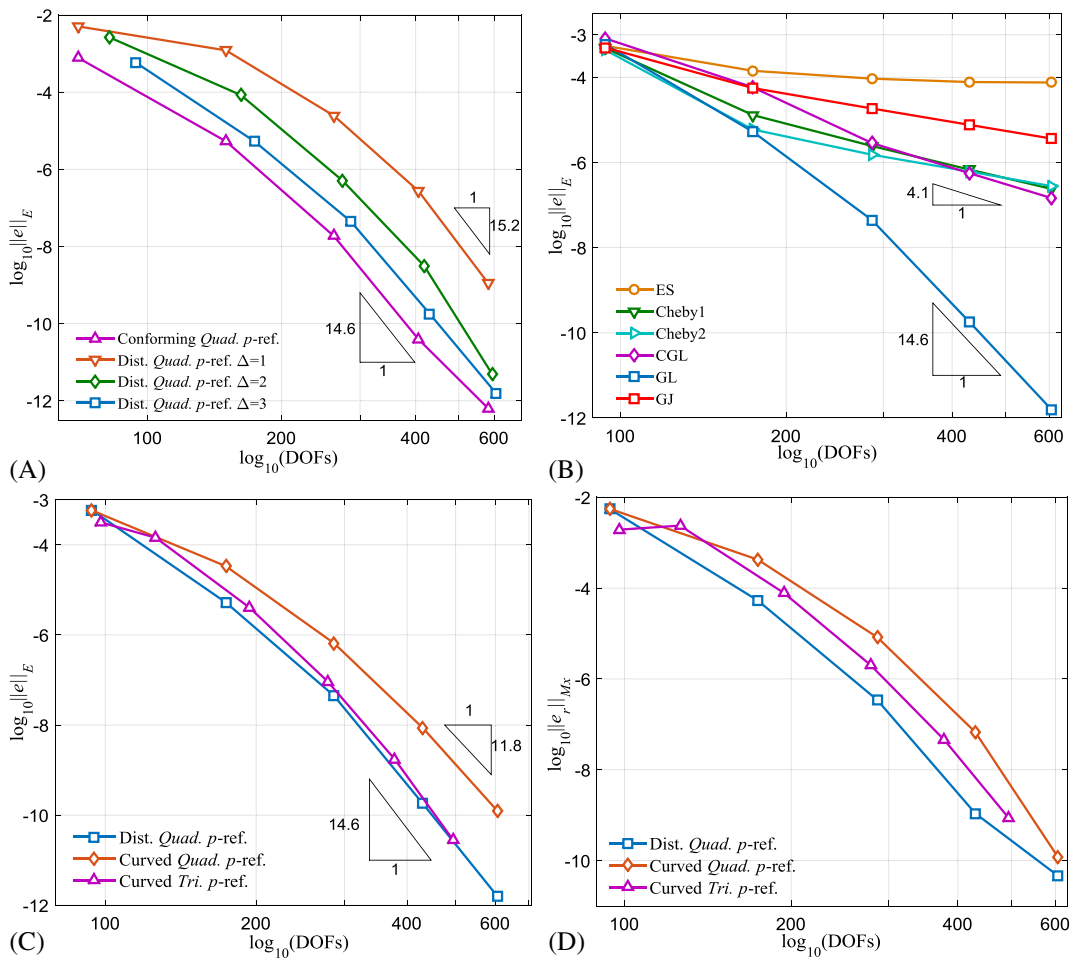


FIGURE 35 Convergence comparison. A, Convergence of the error energy norm for distorted quadrilateral meshes with $\Delta = 1, 2$, and 3 ; B, Convergence of the error energy norm using distorted quadrilateral meshes with various node types and $\Delta = 3$; C, Convergence of the error energy norm using various meshes with $\Delta = 3$; D, Convergence of the relative error of central-point moment M_x . CGL, Chebyshev-Gauss-Lobatto nodes; Cheby1, the first type of Chebyshev nodes; Cheby2, the second type of Chebyshev nodes; DOFs, degrees of freedom; ES, equally spaced nodes; GJ, Gauss-Jacobi nodes; GL, Gauss-Lobatto nodes

quadrilateral mesh with $\Delta = 3$. An exponential convergence rate is only obtained when GL nodes are used. A linear convergence rate is observed when other nonuniform nodes are used, whereas the results of ES nodes seem to diverge. The convergence curves of the error energy norm and the central-point moment that are obtained by various meshes with $\Delta = 3$ are compared in Figures 35C and 35D. Fast convergence is observed in all cases.

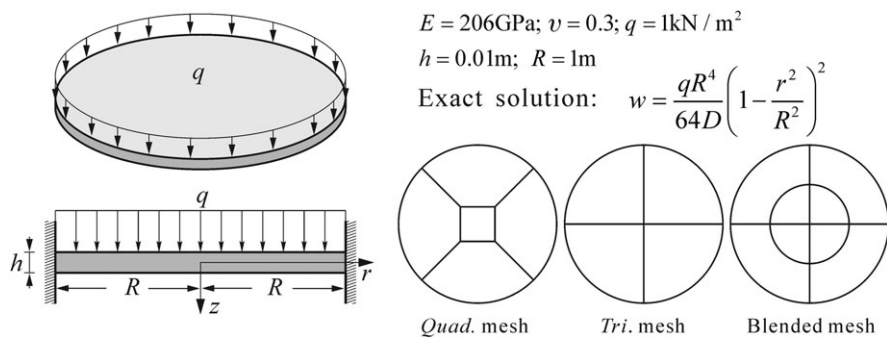


FIGURE 36 Clamped circular plate under a uniformly distributed load

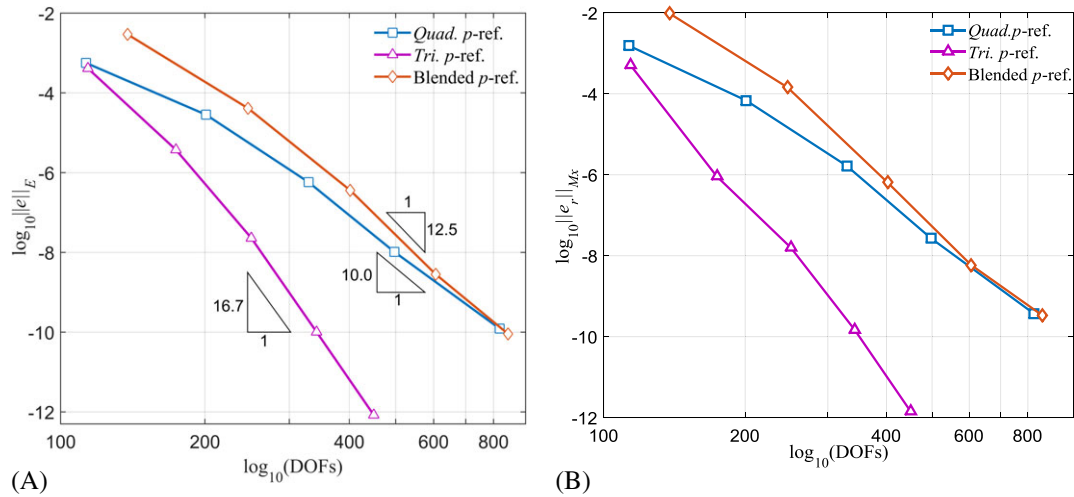


FIGURE 37 Convergence comparison. A, Convergence of the error energy norm using various meshes; B, Convergence of the relative error of the central-point moment [Colour figure can be viewed at wileyonlinelibrary.com]

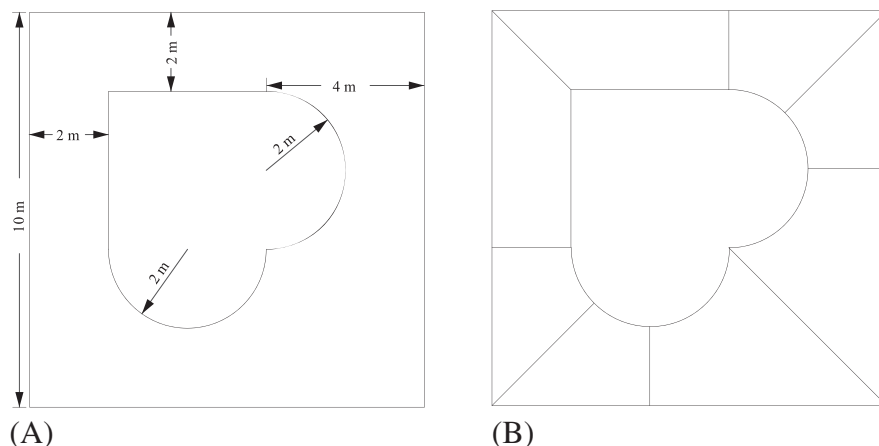


FIGURE 38 Square plate with a complicated cutout. A, Geometric dimensions; B, Mesh

6.3.2 | Bending of a circular plate

The second example is a clamped circular plate that is subjected to a uniformly distributed load (see Figure 36). The exact solution can be found in the work of Reddy.⁴⁷ Three types of meshes, namely, curved quadrilateral mesh, curved triangular mesh, and blended mesh, are used to discretize the domain. GL nodes with $\Delta = 5$ are used for w_n . The convergence curves of the error energy norm and the central-point moment error are shown in Figure 37. Satisfactory convergence is observed. Similar to the results in Figure 28, the results for the triangular mesh converge faster than those for the quadrilateral mesh and the blended mesh because the complete order of the triangular elements is higher compared to the others when the same DOFs are used.

6.3.3 | Plate with an irregular cutout

To evaluate the computational performance of the considered elements in problems with irregular domains, free vibration analysis of a square plate with an irregular cutout (Figure 38A) is employed as our last example. The same mesh as IGA²⁸ is used for domain decomposition (Figure 38B). The first 10 nondimensional frequency parameters, namely, $\Omega = (\omega a^4 \rho h/D)^{1/4}$, for three types of boundary conditions are presented in Table 1. Satisfactory convergence is observed,

TABLE 1 First 10 nondimensional frequency parameters for a square plate with an irregular cutout

N	Mode Sequence									
	1	2	3	4	5	6	7	8	9	10
Simply Supported										
3	4.913	6.389	6.758	8.557	8.973	10.655	10.884	11.600	12.805	13.159
5	4.912	6.388	6.754	8.557	8.966	10.648	10.884	11.599	12.804	13.149
7	4.912	6.388	6.752	8.556	8.963	10.646	10.883	11.599	12.804	13.145
12	4.912	6.388	6.750	8.556	8.960	10.643	10.883	11.599	12.804	13.142
15	4.912	6.388	6.750	8.556	8.960	10.642	10.883	11.599	12.804	13.141
ES-RPIM ⁴⁸	4.905	6.389	6.753	8.574	8.986	10.685	10.897	11.594	12.856	13.223
NS-RPIM ⁴⁸	4.919	6.398	6.775	8.613	9.016	10.738	10.930	11.601	12.903	13.283
IGA ²⁸	5.193	6.579	6.597	7.819	8.812	9.42	10.742	10.776	11.919	13.200
Clamped										
3	7.437	9.819	9.838	10.943	11.157	12.340	12.832	13.446	14.433	14.712
5	7.437	9.817	9.838	10.942	11.153	12.332	12.828	13.438	14.433	14.700
7	7.437	9.817	9.838	10.942	11.151	12.329	12.828	13.438	14.433	14.695
12	7.437	9.816	9.838	10.942	11.149	12.326	12.828	13.438	14.432	14.691
15	7.437	9.816	9.838	10.942	11.148	12.325	12.828	13.438	14.432	14.690
ES-RPIM ⁴⁸	7.423	9.770	9.797	10.927	11.137	12.363	12.822	13.428	14.508	14.789
NS-RPIM ⁴⁸	7.410	9.726	9.764	10.896	11.114	12.353	12.781	13.368	14.485	14.766
IGA ²⁸	7.621	9.810	9.948	11.135	11.216	12.482	12.872	13.650	14.676	14.738
Free										
3	3.223	3.825	4.658	5.473	5.526	6.922	7.331	8.077	8.353	8.664
5	3.222	3.824	4.658	5.473	5.526	6.922	7.328	8.077	8.353	8.664
7	3.222	3.824	4.658	5.473	5.525	6.922	7.327	8.077	8.353	8.664
12	3.222	3.824	4.658	5.473	5.525	6.922	7.326	8.076	8.353	8.664
15	3.222	3.824	4.658	5.473	5.525	6.922	7.325	8.076	8.353	8.664
ES-RPIM ⁴⁸	3.225	3.823	4.646	5.473	5.524	6.902	7.303	8.060	8.349	8.623
NS-RPIM ⁴⁸	3.234	3.846	4.684	5.497	5.547	6.929	7.350	8.103	8.392	8.667
IGA ²⁸	3.482	3.968	5.216	5.805	6.015	7.100	7.485	8.114	8.853	9.001

Abbreviations: ES-RPIM, edge-based smoothing radial-point interpolation method; IGA, isogeometric analysis; NS-RPIM, nodal-based smoothing radial-point interpolation method.

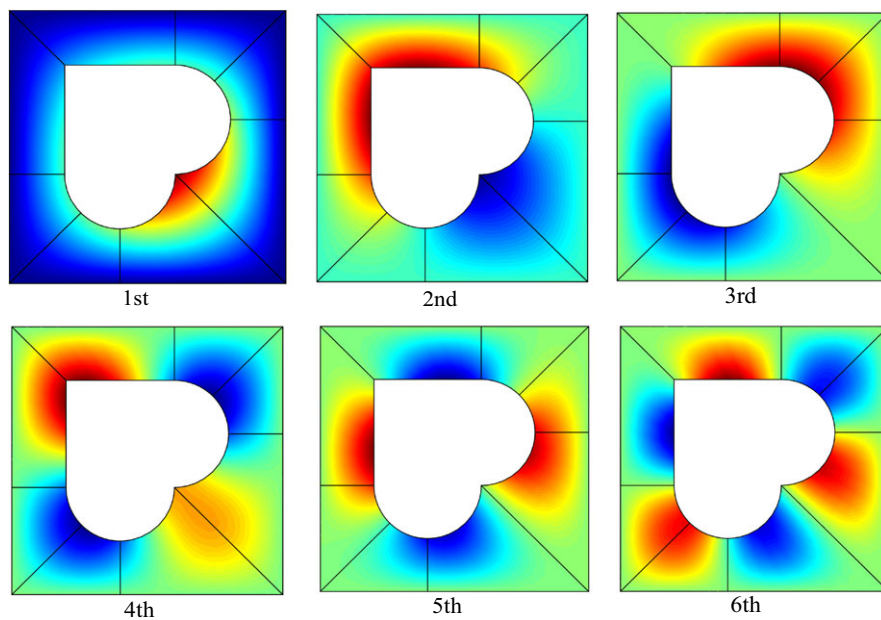


FIGURE 39 First six mode shapes of a simply supported square plate with an irregular cutout ($N = 3$ and $\Delta = 1$)

and the results well agree with the solutions that are obtained via the edge-based smoothing radial-point interpolation method and the nodal-based smoothing radial-point interpolation method.⁴⁸ These results differ slightly from the IGA results,²⁸ where the bending strip method was used to deal with the C^1 conformity. The first six mode shapes of the simply supported plate are presented in Figure 39, where only three nodes for w are used on each edge, and the results exhibit satisfactory smoothness on the element boundaries.

7 | CONCLUSIONS

Both quadrilateral and triangular hierarchical p -version C^1 elements that have curved boundaries were developed in this work via the blending function interpolation method. The features of the elements can be summarized as follows.

1. The hierarchical bases were constructed using the Hermite blending function interpolation methods, along with the Jacobi polynomials. Because of the advantages of blending function interpolation, the approximation orders of the edge bases and internal modes in these elements can differ from each other; hence, local h and p -refinements can be performed conveniently.
2. For convenience in imposing essential boundary conditions and enforcing the C^1 conformity on curved edges, the orthogonal hierarchical bases on the edges of elements were transformed into interpolative nodal bases. Nodal collocation strategies were studied for improving the matrix conditioning. Stable results were obtained, even when very high-order bases were used.
3. For straight-sided triangular elements and parallelograms, the C^1 conformity is fully satisfied. For elements that have curved boundaries, the C^1 conformity is satisfied on nodes and enhanced by GL nodes. Numerical results demonstrated that fast convergence can be realized in both fully conforming elements and elements that have curved boundaries.
4. The developed p -version quadrilateral and triangular elements can be used cooperatively. They are expected to be used in problems with more complicated domains.

In our future work, these elements will be extended to thin-shell analysis with an exact geometry that is created using NURBS or other parameterization methods. The developed elements that have curved boundaries will be very useful not only for the accurate modeling of trimmed surfaces but also for local refinements around the trimmed areas.

ACKNOWLEDGEMENT

We gratefully acknowledge the financial support from the National Natural Science Foundation of China under grants 11772031, 11402015, 11372021, and 11172028.

ORCID

Yufeng Xing  <https://orcid.org/0000-0001-6426-5188>

Bo Liu  <https://orcid.org/0000-0001-7844-9981>

REFERENCES

1. Zienkiewicz OC, Taylor RL, Zhu JZ. *The Finite Element Method: Its Basis and Fundamentals*. New York, NY: Elsevier; 2013.
2. Oñate E. *Structural Analysis With the Finite Element Method. Linear statics: Volume 2: Beams, Plates and Shells*. Barcelona, Spain: Springer; 2013.
3. Holdeman JT, Kim JW. Computation of incompressible thermal flows using Hermite finite elements. *Comput Methods Appl Mech Eng*. 2010;199(49):3297-3304.
4. Hrabok MM, Hrudey TM. A review and catalogue of plate bending finite elements. *Comput Struct*. 1984;19(3):479-495.
5. Dau F, Polit O, Touratier M. An efficient C₁ finite element with continuity requirements for multilayered/sandwich shell structures. *Comput Struct*. 2004;82(23):1889-1899.
6. Holdeman JT. A Hermite finite element method for incompressible fluid flow. *Int J Numer Meth Fluids*. 2010;64(4):376-408.
7. Watkins DS. On the construction of conforming rectangular plate elements. *Int J Numer Methods Eng*. 1976;10(4):925-933.
8. Lesičar T, Sorić J, Tonković Z. Large strain, two-scale computational approach using C₁ continuity finite element employing a second gradient theory. *Comput Methods Appl Mech Eng*. 2016;298:303-324.
9. Babuska I, Szabo BA, Katz IN. The p-version of the finite element method. *SIAM J Numer Anal*. 1981;18(3):515-545.
10. Stein E, Borst RD, Hughes TJR. *Encyclopedia of Computational Mechanics. Volume 1: Fundamentals*. 1st ed. Vol 1. Chichester, UK: John Wiley & Sons; 2004.
11. Peano A. Hierarchies of conforming finite elements for plane elasticity and plate bending. *Comput Math Appl*. 1976;2(3):211-224.
12. Wang DW, Katz IN, Szabo BA. Implementation of a C₁ triangular element based on the p-version of the finite element method. *Comput Struct*. 1984;19(3):381-392.
13. Chinosis C, Scapolla T, Sacchi G. A hierachic family of C¹ finite elements for 4th order elliptic problems. *Comput Mech*. 1991;8(3):181-191.
14. Bardell NS. Free vibration analysis of a flat plate using the hierarchical finite element method. *J Sound Vib*. 1991;151(2):263-289.
15. Bardell NS. The free vibration of skew plates using the hierarchical finite element method. *Comput Struct*. 1992;45(5-6):841-874.
16. Dhatt G, Touzot G, Lefrançois E. *Finite Element Method*. Hoboken, NJ: John Wiley & Sons; 2012.
17. Beslin O, Nicolas J. A hierarchical functions set for predicting very high order plate bending modes with any boundary conditions. *J Sound Vib*. 1997;202(5):633-655.
18. Xing Y, Liu B. High-accuracy differential quadrature finite element method and its application to free vibrations of thin plate with curvilinear domain. *Int J Numer Methods Eng*. 2009;80(13):1718-1742.
19. Zhong HZ, Yue ZG. Analysis of thin plates by the weak form quadrature element method. *Sci China Phys Mech Astron*. 2012;55(5):861-871.
20. Jin C, Wang X. Weak form quadrature element method for accurate free vibration analysis of thin skew plates. *Comput Math Appl*. 2015;70(8):2074-2086.
21. Ferreira LJF, Bittencourt ML. Hierarchical high-order conforming C¹ bases for quadrangular and triangular finite elements. *Int J Numer Methods Eng*. 2017;109(7):936-964.
22. Bernadou M, Boisserie JM. Curved finite elements of class C₁: implementation and numerical experiments. Part 1: construction and numerical tests of the interpolation properties. *Comput Methods Appl Mech Eng*. 1993;106(1):229-269.
23. Gao Q, Li L. Interpolated boundary conditions in plate bending problems using C₁ curved finite elements. *Comput Methods Appl Mech Eng*. 1997;148(3):235-255.
24. Hughes TJR, Cottrell JA, Bazilevs Y. Isogeometric analysis: CAD, finite elements, NURBS, exact geometry and mesh refinement. *Comput Methods Appl Mech Eng*. 2005;194(39):4135-4195.
25. Cottrell JA, Hughes TJR, Reali A. Studies of refinement and continuity in isogeometric structural analysis. *Comput Methods Appl Mech Eng*. 2007;196(41-44):4160-4183.
26. Kiendl J, Bletzinger KU, Linhard J, Wüchner R. Isogeometric shell analysis with Kirchhoff-love elements. *Comput Methods Appl Mech Eng*. 2009;198(49):3902-3914.
27. Kiendl J, Bazilevs Y, Hsu MC, Wüchner R, Bletzinger KU. The bending strip method for isogeometric analysis of Kirchhoff-love shell structures comprised of multiple patches. *Comput Methods Appl Mech Eng*. 2010;199(37-40):2403-2416.
28. Shojaae S, Izadpanah E, Valizadeh N, Kiendl J. Free vibration analysis of thin plates by using a NURBS-based isogeometric approach. *Finite Elem Anal Des*. 2012;61:23-34.

29. Guo Y, Ruess M. Nitsche's method for a coupling of isogeometric thin shells and blended shell structures. *Comput Methods Appl Mech Eng.* 2015;284:881-905.
30. Guo Y, Heller J, Hughes TJR, Ruess M, Schillinger D. Variationally consistent isogeometric analysis of trimmed thin shells at finite deformations, based on the STEP exchange format. *Comput Methods Appl Mech Eng.* 2018;336:39-79.
31. Liu B, Xing Y, Wang Z, Lu X, Sun H. Non-uniform rational Lagrange functions and its applications to isogeometric analysis of in-plane and flexural vibration of thin plates. *Comput Methods Appl Mech Eng.* 2017;321:173-208.
32. Gordon WJ. Blending-function methods of bivariate and multivariate interpolation and approximation. *SIAM J Numer Anal.* 1971;8(1):158-177.
33. Gordon WJ, Hall CA. Transfinite element methods: blending-function interpolation over arbitrary curved element domains. *Numer Math.* 1973;21(2):109-129.
34. Webb JP, Abouachra R. Hierarchical triangular elements using orthogonal polynomials. *Int J Numer Methods Eng.* 1995;38(2):245-257.
35. Houmat A. In-plane vibration of plates with curvilinear plan-forms by a trigonometrically enriched curved triangular p-element. *Thin-Walled Struct.* 2008;46(2):103-111.
36. Pavel S, Karel S, Ivo D. *Higher-Order Finite Element Methods*. Boca Raton, FL: Chapman & Hall/CRC; 2004.
37. Shu C. *Differential Quadrature and Its Application in Engineering*. London, UK: Springer-Verlag; 2000.
38. Liu C, Liu B, Xing Y, Reddy JN, Neves AMA, Ferreira AJM. In-plane vibration analysis of plates in curvilinear domains by a differential quadrature hierarchical finite element method. *Meccanica*. 2016;52(4):1017-1033.
39. Liu C, Liu B, Zhao L, Xing Y, Ma C, Li H. A differential quadrature hierarchical finite element method and its applications to vibration and bending of Mindlin plates with curvilinear domains. *Int J Numer Methods Eng.* 2016;109(2):174-197.
40. Liu B, Xing Y, Wang W, Yu W. Thickness-shear vibration analysis of circular quartz crystal plates by a differential quadrature hierarchical finite element method. *Compos Struct.* 2015;131:1073-1080.
41. Bos L, Taylor MA, Wingate BA. Tensor product Gauss-Lobatto points are Fekete points for the cube. *Math Comput.* 2001;70(236):1543-1547.
42. Sevilla R, Fernández-Méndez S, Huerta A. NURBS-enhanced finite element method (NEFEM). *Arch Comput Methods Eng.* 2011;18(4):441.
43. Taylor MA, Vincent RE, Wingate BA. An algorithm for computing Fekete points in the triangle. *SIAM J Numer Anal.* 2000;38(5):1707-1720.
44. Cowper GR, Kosko E, Lindberg GM, Olson MD. Static and dynamic applications of a high-precision triangular plate bending element. *AIAA J.* 1969;7(10):1957-1965.
45. Ivannikov V, Tiago C, Pimenta PM. Generalization of the C1 TUBA plate finite elements to the geometrically exact Kirchhoff-love shell model. *Comput Methods Appl Mech Eng.* 2015;294:210-244.
46. Tornabene F, Fantuzzi N, Bacciochi M, Viola E. *Laminated Composite Doubly-Curved Shell Structures: Differential and Integral Quadrature Strong Formulation Finite Element Method*. Bologna, Italy: Società Editrice Esculapio; 2016.
47. Reddy JN. *Theory and Analysis of Elastic Plates and Shells*. 2nd ed. New York, NY: CRC Press; 2006.
48. Cui XY, Liu GR, Li GY, Zhang GY. A thin plate formulation without rotation DOFs based on the radial point interpolation method and triangular cells. *Int J Numer Methods Eng.* 2011;85(8):958-986.

How to cite this article: Wu Y, Xing Y, Liu B. Hierarchical p -version C^1 finite elements on quadrilateral and triangular domains with curved boundaries and their applications to Kirchhoff plates. *Int J Numer Methods Eng.* 2019;119:177–207. <https://doi.org/10.1002/nme.6046>

APPENDIX

SHAPE FUNCTIONS

	Quadrilateral Elements	Triangular Elements
Vertex 1	$S_{w_1}^{V_1} = h_2(\xi)H_1(\eta) + H_1(\xi)h_2(\eta) - h_2(\xi)h_2(\eta)$ $S_{w_\xi}^{V_1} = H_1^{(1)}(\xi)h_2(\eta); S_{w_\eta}^{V_1} = h_2(\xi)H_1^{(1)}(\eta)$ $S_{w_{\xi\xi}}^{V_1} = H_1^{(2)}(\xi)h_2(\eta); S_{w_{\eta\eta}}^{V_1} = h_2(\xi)H_1^{(2)}(\eta);$ $S_{w_{\xi\eta}}^{V_1} = h_1(\xi)h_1(\eta)$	$S_w^{V_1} = 6\xi^5 - 5\xi^2(3\xi^2 - 2\xi - 6\xi\eta + 6\xi\eta\xi), \zeta = 1 - \xi - \eta$ $S_{w_\xi}^{V_1} = \xi(3\xi + 1)\xi^2(3\eta + \zeta); S_{w_\eta}^{V_1} = \eta(3\eta + 1)\xi^2(3\xi + \zeta)$ $S_{w_{\xi\xi}}^{V_1} = \xi^2\xi^2(3\eta + \zeta)/2; S_{w_{\eta\eta}}^{V_1} = \eta^2\xi^2(3\xi + \zeta)/2; S_{w_{\xi\eta}}^{V_1} = \xi\eta\xi^2;$
Vertex 2	$S_w^{V_2} = h_3(\xi)H_1(\eta) + H_2(\xi)h_2(\eta) - h_3(\xi)h_2(\eta)$ $S_{w_\xi}^{V_2} = H_2^{(1)}(\xi)h_2(\eta); S_{w_\eta}^{V_2} = h_3(\xi)H_1^{(1)}(\eta)$ $S_{w_{\xi\xi}}^{V_2} = H_2^{(2)}(\xi)h_2(\eta); S_{w_{\eta\eta}}^{V_2} = h_3(\xi)H_1^{(2)}(\eta);$ $S_{w_{\xi\eta}}^{V_2} = h_4(\xi)h_1(\eta)$	$S_w^{V_2} = \xi^3(6\xi^2 - 15\xi + 10); S_{w_\xi}^{V_2} = -\xi^3(3\xi^2 - 7\xi + 4)$ $S_{w_\eta}^{V_2} = \xi^2\eta(9\xi\eta - 9\eta - 2\xi + 6\eta^2 + 3); S_{w_{\xi\xi}}^{V_2} = \xi^3(\xi - 1)^2/2$ $S_{w_{\eta\eta}}^{V_2} = \xi^2\eta^2(3\xi + 2\eta - 2)/2; S_{w_{\xi\eta}}^{V_2} = -\xi^2\eta(3\xi\eta - 3\eta - \xi + 2\eta^2 + 1)$
Vertex 3	$S_w^{V_3} = h_3(\xi)H_2(\eta) + H_2(\xi)h_3(\eta) - h_3(\xi)h_3(\eta)$ $S_{w_\xi}^{V_3} = H_2^{(1)}(\xi)h_3(\eta); S_{w_\eta}^{V_3} = h_3(\xi)H_2^{(1)}(\eta)$ $S_{w_{\xi\xi}}^{V_3} = H_2^{(2)}(\xi)h_3(\eta); S_{w_{\eta\eta}}^{V_3} = h_3(\xi)H_2^{(2)}(\eta);$ $S_{w_{\xi\eta}}^{V_3} = h_4(\xi)h_4(\eta)$	$S_w^{V_3} = \eta^3(6\eta^2 - 15\eta + 10); S_{w_\xi}^{V_3} = \eta^2\xi(9\xi\eta - 9\xi - 2\eta + 6\xi^3 + 3);$ $S_{w_\eta}^{V_3} = -\eta^3(3\eta^2 - 7\eta + 4); S_{w_{\xi\xi}}^{V_3} = \eta^2\xi^2(3\eta + 2\xi - 2)/2;$ $S_{w_{\eta\eta}}^{V_3} = \eta^3(1 - \eta)^2/2; S_{w_{\xi\eta}}^{V_3} = -\eta^2\xi(3\xi\eta - 3\xi - \eta + 2\xi^2 + 1)$
Vertex 4	$S_w^{V_4} = h_2(\xi)H_2(\eta) + H_1(\xi)h_3(\eta) - h_2(\xi)h_3(\eta)$ $S_{w_\xi}^{V_4} = H_1^{(1)}(\xi)h_3(\eta); S_{w_\eta}^{V_4} = h_2(\xi)H_2^{(1)}(\eta);$ $S_{w_{\xi\xi}}^{V_4} = H_1^{(2)}(\xi)h_3(\eta); S_{w_{\eta\eta}}^{V_4} = h_2(\xi)H_2^{(2)}(\eta);$ $S_{w_{\xi\eta}}^{V_4} = h_1(\xi)h_4(\eta)$	—
Edge 1	$S_{w,i}^{S_1} = (1 + \xi)^3(1 - \xi)^3 J_i^{(4,4)}(\xi)h_2(\eta); i = 0 \sim M - 1$ $S_{w_\xi,i}^{S_1} = (1 + \xi)^2(1 - \xi)^2 J_i^{(4,4)}(\xi)h_1(\eta); i = 0 \sim M$	$S_{w,i}^{S_1}(\xi) = \xi^3\xi^2(3\eta + \zeta)J_i^{(7,6)}(2\xi - 1), i = 0 \sim M - 1$ $S_{w_\xi,i}^{S_1}(\xi) = \xi^2\eta\xi^2 J_i^{(7,4)}(2\xi - 1), i = 0 \sim M$
Edge 2	$S_{w,i}^{S_2} = (1 - \eta)^3(1 + \eta)^3 J_i^{(4,4)}(\eta)h_3(\xi); i = 0 \sim N - 1$ $S_{w_\xi,i}^{S_2} = (1 - \eta)^2(1 + \eta)^2 J_i^{(4,4)}(\eta)h_4(\xi); i = 0 \sim N$	$S_{w,i}^{S_2}(\eta) = -\xi^2\eta^3(\xi + 3\zeta)J_i^{(7,6)}(2\eta - 1), i = 0 \sim N - 1$ $S_{w_\xi,i}^{S_2}(\eta) = -\xi^2\eta^2\xi J_i^{(7,4)}(2\eta - 1), i = 0 \sim N$
Edge 3	$S_{w,i}^{S_3} = (1 - \xi)^3(1 + \xi)^3 J_i^{(4,4)}(\xi)h_3(\eta); i = 0 \sim P - 1$ $S_{w_\xi,i}^{S_3} = (1 - \xi)^2(1 + \xi)^2 J_i^{(4,4)}(\xi)h_4(\eta); i = 0 \sim P$	$S_{w,i}^{S_3}(\eta) = \eta^3\xi^2(3\xi + \zeta)J_i^{(7,6)}(2\eta - 1), i = 0 \sim P - 1$ $S_{w_\xi,i}^{S_3}(\eta) = \xi\eta^2\xi^2 J_i^{(7,4)}(2\eta - 1), i = 0 \sim P$
Edge 4	$S_{w,i}^{S_4} = (1 - \eta)^3(1 + \eta)^3 J_i^{(4,4)}(\eta)h_2(\xi); i = 0 \sim Q - 1$ $S_{w_\xi,i}^{S_4} = (1 - \eta)^2(1 + \eta)^2 J_i^{(4,4)}(\eta)h_1(\xi); i = 0 \sim Q$	—
Face	$S_{mn}^F = C_{mn}(1 - \xi^2)^2(1 - \eta^2)^2 J_{m-1}^{(4,4)}(\xi)J_{n-1}^{(4,4)}(\eta);$ $m = 1 \sim H_\xi, n = 1 \sim H_\eta$	$S_{pn}^F(\xi, \eta) = C_{pn}\xi^2\xi^2\eta^2(1 - \eta)^{p-n-6} J_{p-n-6}^{(4,4)}\left(\frac{2\xi}{1 - \eta} - 1\right) J_n^{(2p-2n-3,4)}(2\eta - 1);$ $p \geq 6, n = 0 \sim p - 6$